Modeling the Motion of Microcapsules on Compliant Polymeric Surfaces

Alexander Alexeev, Rolf Verberg, and Anna C. Balazs*

Chemical Engineering Department, University of Pittsburgh, Pittsburgh, Pennsylvania 15261

Received July 22, 2005; Revised Manuscript Received October 3, 2005

ABSTRACT: By integrating mesoscale models for hydrodynamics and micromechanics, we examine the fluid-driven motion of microcapsules on compliant surfaces. The capsules, modeled as fluid-filled elastic shells, represent polymeric microcapsules or biological cells. We examine the motion of these capsules on flat, mechanically uniform surfaces, mechanically patterned surfaces that contain alternating regions of hard and soft domains, and topologically patterned surfaces, i.e., a corrugated substrate and a substrate that encompasses a regular array of compliant posts. We isolate conditions where the mechanically and topographically patterned surfaces can transmit "stop" and "go" instructions, causing the capsules to halt at specific locations on the substrate, and with an increase in the imposed flow velocity, to resume moving. In the case of the corrugated surfaces, varying the size of the asperities permits significant control over the translational velocity of a capsule for a given shear rate. For surfaces containing regular arrays of compliant posts, the substrates also affect the capsules' gait, causing them to "crawl", "walk", or "jump". The latter behavior could promote the intermixing of reactants that are encapsulated within the microcapsules. These topographically patterned surfaces can also be utilized to sort capsules accordingly their size. Such control over capsule dynamics can enable the fabrication of arrays of mobile microreactors and facilitate various biological assays.

Introduction

The development of microreactors, which involve the manipulation of minute quantities of reagents in micron-scale "flasks", could vastly increase the speed at which large amounts of new chemical information can be obtained.[1] To realize this potential, researchers recently created droplet-based microfluidic devices, where micron-sized aqueous droplets are propelled by electric fields to move on a planar substrate.[2] The entire assembly is immersed in a chamber that is filled with air or a liquid that is immiscible with the droplet. By applying voltages across specific electrodes on the surface, droplets are driven to move, merge, mix their contents, and split into smaller drops.[2d] However, one limitation of this approach is that the range of chemical components or reactions that can be confined within aqueous drops is fairly restricted. In contrast, microcapsules that are composed of a thin polymeric shell and an encapsulated fluid constitute robust[3,4,5] and versatile carriers and offer a range of advantages over pure fluid drops. In particular, a vast variety of compounds can be encapsulated within these microcapsules,[6] and the assembly has significant storage stability.[7] Both the exterior and interior of the polymeric shell can be chemically tailored, and reagents can even be grown within the interior of the capsule.[8] The permeability of the microcapsule can be controlled in a straightforward manner[9] by modifying the external solution (e.g., by varying pH[10] or adding organic solvents[11]). In addition, microcapsules can be driven to undergo fusion,[4b,12] allowing the contents of different capsules to be intermixed. For these reasons, the capsules constitute promising micron-sized reaction flasks. However, the reaction surfaces described above were designed to propel simple fluid drops.[2] To create highly effective microreactors, it would be optimal to integrate the robust microcapsules with "smart" surfaces, which can regulate the motion of the capsules.

* To whom correspondence should be addressed: e-mail balazs1@engr.pitt.edu.

To design such smart surfaces, one needs efficient computational models that capture not only the interactions between the polymeric shell and the bounding fluids but also the interactions between the microcapsule and the substrate. To address this need, we herein integrate two mesoscale approaches to model a fluid-filled elastic shell that is immersed in a host solution and driven to move on a compliant surface. In our hybrid approach, the fluid dynamics are captured via the lattice Boltzmann model (LBM), an efficient solver for the Navier−Stokes equation.[13] The behavior of the elastic shell is simulated via the lattice spring model (LSM), which consists of a network of harmonic springs connecting regularly spaced masses.[14] Our integrated LBM/LSM approach allows for a dynamic interaction between the elastic walls and the surrounding fluid. In other words, dynamically and interactively, the moving walls exert a force on the fluid and, in turn, the fluid reacts back on the walls. We recently used this method to examine the collision of fluid-filled elastic shells with a hard, flat wall in a vacuum.[15] To model a fluid-driven capsule interacting with a compliant surface, we introduce a host fluid and an elastic substrate, which are modeled via the LBM and the LSM, respectively. We also modify the previous model in order to accurately describe thin polymeric shells. With these modifications to our earlier model, we can now probe the dynamic interactions among all the components in the system: the host solution, the encapsulated fluid, the bounding elastic shell, and the compliant surface.

We note that such fluid-filled elastic shells also serve as simple models for biological cells (e.g., leukocytes). In this context, researchers have carried out computational studies of the cell's motion along substrates.[16−18] What is unique to our simulations is that we examine how the substrate's compliance and topography affect the cell's movement. In particular, through the LSM, we can modify the stiffness of the substrate and thus model soft surfaces. An important reason for focusing on compliant surfaces is that recent advances in soft

10.1021/ma0516135 CCC: $30.25
Published on Web 11/05/2005

lithography make it possible to significantly tailor the surface of polymeric materials,[19–21] making them the ideal systems for creating smart substrates. As we show below, simple mechanical or topographical patterning of these soft surfaces permits significant control over the motion of capsules (i.e., synthetic microcapsules or biological cells). In particular, we isolate systems that affect not only the capsule's velocity but also its specific "gait" or way of moving along the surface. In addition, we uncover surface patterns that drive the capsules to stop at specified locations along the interfaces; with small changes in the velocity of the imposed flow, the capsules can be made to resume their motion.

The findings from these studies yield guidelines for creating smart surfaces that could manipulate the microcapsule's motion, for example, directing these carriers to deliver their encapsulated "payload" to specified locations on the substrate. The results can also provide design rules for creating active substrates for regulating the in vitro trafficking of cells, allowing the fluid-driven cells to be readily sorted or isolated and thereby facilitating biological assays and tissue engineering studies.[22]

We emphasize that the LSM captures the behavior of an elastic, deformable solidlike material (or with addition of a dissipative unit between the springs, a viscoelastic material[23]); thus, the shells in our systems are also considered to be solidlike, as opposed to being fluidlike. Consequently, the systems that are most appropriately modeled here are the microcapsules whose shells are formed, for example, from multiple layers of polyelectrolytes (i.e., through a layer-by-layer deposition process).[3] The approach is also appropriate for modeling polymersomes, where the high-molecular-weight polymers used to create the vesicles are entangled and crosslinked in order to enhance the mechanical integrity of the entity.[4] In the case of white blood cells, or leukocytes, the cytoskeleton acts to reinforce the plasma membrane, and thus, the cell's outer casing can also be modeled as an elastic layer.[17] Our approach, however, may not be appropriate for capturing the behavior of vesicles formed from short-chain lipids since the lipid layer is commonly considered to be a dynamic, fluidlike like entity.[4,24]

Below, we describe the LBM/LSM model in more detail. We then present our findings on the effects of surface compliance and topography on the fluid-driven motion of the capsules on these surfaces.

Methodology

We take advantage of our recently developed hybrid approach, which involves a coupling of the lattice Boltzmann and lattice spring methods.[15] Unlike conventional numerical schemes, which involve a direct discretization of the continuum equations,[25] these lattice models are used to simulate the underlying physical processes that give rise to the appropriate continuum behavior. We recently validated our integrated LBM/LSM model by determining the "breathing modes" of a fluid-filled elastic shell and found good agreement with analytical theory.[15] We also examined the interactions between the fluid-filled shell and a hard, flat surface in a vacuum.[15] As we detail below, we extend the model to encompass an external solvent, an imposed flow field, and a compliant substrate. We also modify the previous model in order to accurately describe thin shells.

Below, we first describe the individual components of the approach and then detail how these components are integrated to capture interactions among the elastic shell, the surrounding fluid, and the substrate. We also discuss how we validated the new model.

Lattice Boltzmann Model. As noted above, the lattice Boltzmann model is a lattice-based method for simulating hydrodynamic flows. The model consists of two processes: the first being the propagation of fluid "particles" to neighboring lattice sites and the second being collisions between particles when they reach a site. The system is characterized by a single particle velocity distribution function, $f_i(\mathbf{r},t) \equiv f(\mathbf{r},\mathbf{c}_i,t)$, describing the mass density of fluid particles with velocity $\mathbf{c}_i$ at a lattice node $\mathbf{r}$ at time t. Here, $\mathbf{c}_i$, $\mathbf{r}$, and t are discrete variables, while the distribution function itself is a continuous variable. The hydrodynamic quantities are moments of the distribution function, i.e., the mass density $\rho = \sum_i f_i$, the momentum density $\mathbf{j} = \rho\mathbf{u} = \sum_i \mathbf{c}_i f_i$, with $\mathbf{u}$ being the local fluid velocity, and the momentum flux $\Pi = \sum_i \mathbf{c}_i \mathbf{c}_i f_i$. The time evolution of the distribution function is governed by the discretized Boltzmann equation[26]

$$f_i(\mathbf{r} + \mathbf{c}_i\Delta t,\, t + \Delta t) = f_i^*(\mathbf{r},t) = f_i(\mathbf{r},t) + \Omega[\mathbf{f}(\mathbf{r},t)] \tag{1}$$

To illustrate the two steps (collisions and propagation), we define $f_i^*(\mathbf{r},t)$ as the postcollision distribution function.

The collision operator, $\Omega[\mathbf{f}(\mathbf{r},t)]$, accounts for the change in f_i due to instantaneous collisions at the lattice nodes; its action depends on all the f_i's at a node, denoted collectively by $\mathbf{f}(\mathbf{r},t)$. We adopt a multirelaxation time collision operator,[27] which, in contrast to the more widely employed single relaxation time collision operator, enables us to assign independent values to the shear and bulk viscosities. This collision operator conserves mass and momentum and relaxes the momentum flux (or stress) toward local equilibrium.

The velocity $\mathbf{c}_i$ in the ith direction is chosen such that fluid particles propagate from one lattice site to the next in exactly one time step Δt. The nine velocities of our two-dimensional model correspond to movement to the nearest- and next-nearest-neighbor directions of a simple square lattice and to rest particles. This model is a straightforward projection onto two dimensions of the three-dimensional model that was discussed in detail in ref 15. In this paper, all dimensional parameters are expressed in terms of the lattice Boltzmann units for the lattice spacing, Δx, and the time step, Δt, where both values are taken to be unity.

Lattice Spring Model. The solid, elastic material is represented by a lattice spring model, which consists of a network of harmonic springs that connect regularly spaced mass points or nodes. The elastic energy associated with a node at position $\mathbf{r}_i$ is given by

$$E(\mathbf{r}_i) = \frac{1}{2}\sum_j k_j (r_{ij} - r_{ij}^{\mathrm{eq}})^2 \tag{2}$$

where the summation runs over all nearest- and next-nearest-neighbor nodes. Here, $r_{ij} = |\mathbf{r}_i - \mathbf{r}_j|$ is the length of the spring between two nodes with positions $\mathbf{r}_i$ and $\mathbf{r}_j$, r_{ij}^{eq} is its equilibrium length, and k_j is its spring constant.[14] This results in a spring force $\mathbf{F}_S$ on node $\mathbf{r}_i$ of the form

$$\mathbf{F}_S(\mathbf{r}_i) = -\sum_j k_j \left(\frac{r_{ij} - r_{ij}^{eq}}{r_{ij}} \right) \mathbf{r}_{ij} \quad (3)$$

To capture the dynamics of the solid material, we assign a mass M_i to each node $\mathbf{r}_i$ and integrate Newton's equation of motion, $\mathbf{F}(\mathbf{r}_i) = M_i(\partial^2\mathbf{r}_i/\partial t^2)$, where $\mathbf{F}$ is the total force acting on the node. A friction term could be introduced within the above equation to account for dissipation. The total force $\mathbf{F}$ consists of the spring force in eq 3 and the force exerted by the fluid on the solid at the solid−fluid boundary, discussed in more detail below. We utilize the velocity Verlet algorithm to integrate Newton's equation of motion. This is a well-known molecular dynamics algorithm that updates the positions, velocities, and accelerations of each node in discrete time steps.[28]

Our system has different solid domains: the compliant, underlying substrate, and the compliant shells of the individual microcapsules (see schematic in Figure 1). The substrate consists of a simple square lattice, where eight springs connect each node with its nearest- and next-nearest neighbors. The spring constants are k_1 and $k_{\sqrt{2}}$ in the orthogonal and the diagonal directions, respectively. In this model, the values for the masses of nodes at the solid−fluid interface and the spring constants of the corresponding, interconnecting springs are half the values of their bulk counterparts. This represents a modification of our earlier model,[15] where these masses and springs are equal in value to those in the bulk. This modification facilitates our new implementation of the solid−fluid boundary condition by placing the solid−fluid interface at the actual nodal positions.[14b]

For small deformations and $^1/_2 k_1 = k_{\sqrt{2}} \equiv k$, this system of equations can be shown to obey linear elasticity theory and results in a Young's modulus $E = 5k/2\Delta x_{LS}$ and a speed of sound $c_s = \Delta x_{LS}\sqrt{3k/M}$, with Δx_{LS} being the lattice spacing in the LSM.[14] The solid density is then given by $\rho_s = M/\Delta x_{LS}^3$. This simple model is restricted to a Poisson's ratio of $\nu = ^1/_4$, although more complicated many-body interactions can be included in order to vary ν.[29]

As noted above, the capsule's compliant shell constitutes the other solid domain in our system. To accurately represent a thin shell, we model this membrane by a cylindrically symmetric lattice of springs, consisting of n concentric layers of N nodes that lay a distance Δr apart. We again use $^1/_2 k_1 = k_{\sqrt{2}} \equiv k$ for springs connecting nearest- and next-nearest neighbors, while nodes and springs at the surface are treated as they are for the substrate, resulting in a shell thickness $h = (n - 1)\Delta r$. The distance Δx_{LS} between the nodes in each layer is such that $\Delta x_{LS} = \Delta r = 2\pi(R - h/2)/N$, with R being the outer radius of the shell. For small deformations, $R \gg \Delta x_{LS}$ and $R \gg h$, this results in a Young's modulus and speed of sound given by expressions identical to those for the square lattice. We note that, depending on the desired spatial resolution, we can choose different values of Δx_{LS} for the shell and the substrate. Furthermore, we can use different spring constants and masses in each of the domains.

The Verlet algorithm that we use to integrate Newton's equation of motion is explicit in time. For stability purposes, this requires that we choose a lattice spacing, Δx_{LS}, and time step, Δt_{LS}, in the lattice spring part of the code such that the Courant number $Cr = c_s\Delta t_{LS}/\Delta x_{LS}$ is smaller than one.[13] Furthermore, we need to maintain $\Delta x_{LS} \geq \Delta x$, which prevents large fluctuations in the force of the fluid on the lattice spring nodes due to the discretization. In our applications, we set $\Delta t_{LS} = \Delta t = 1$ (equal to the time step in the lattice Boltzmann part of the code), while $\Delta x_{LS} \approx 1.2\Delta x$ and $\Delta x = 1$. This allows us to satisfy the Courant condition for the entire range of c_s that was used to obtain our results. However, in the validation section, we use a few combinations of Δx_{LS} and c_s that result in $Cr > 1$ for $\Delta t_{LS} = 1$. In these cases, we perform several (two to five) lattice spring iterations for each lattice Boltzmann cycle, thus reducing Δt_{LS} sufficiently to stabilize the simulations.

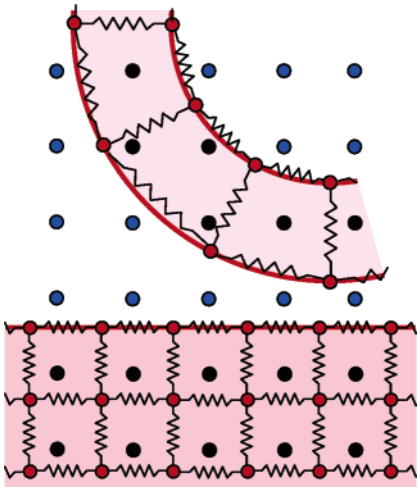

Figure 1. Schematic of our system. The nodes that are connected by springs form the lattice spring lattice (for clarity, we omitted the diagonal springs that connect each node with all its next-nearest neighbors). The remaining nodes represent the lattice Boltzmann lattice (blue for fluid nodes and black for solid nodes). The solid lines are the solid−fluid interfaces.

Solid−Fluid Boundary Condition. To capture the interactions between the solids and fluids, lattice spring nodes that are situated at the solid−fluid interface must impose velocities on the surrounding fluids through boundary conditions and, in turn, experience forces due to the fluid pressure and viscous stresses. Put concisely, the simulation proceeds through the sequential update of both the lattice spring and the lattice Boltzmann systems. The LSM system is updated by first calculating the forces that are acting on the LSM nodes, due to the LSM springs, the enclosed fluid, and the surrounding solvent. New positions, velocities, and accelerations of the LSM nodes are then calculated using the Verlet algorithm. In updating the LBM system, we first establish which LBM links intersect the solid/fluid interface. We then obtain the velocities at these points of intersection from neighboring LSM nodes. Next, we propagate the distribution function by streaming fluid particles to their neighboring nodes whenever these nodes are in the fluid domain, and otherwise, we apply the appropriate boundary condition (described below). Finally, we modify the distribution functions at the LBM nodes to account for the collision step. We then repeat the entire cycle. Below, we describe in more detail how these processes are specifically carried out.

In our current implementation, fluid particles that are moving on a link that intersects the solid−fluid interface are bounced back into the fluid phase at the intersection point (or boundary node) $\mathbf{r}_b$, as illustrated in Figure 2. Here, $\delta_1 = |\mathbf{r}_1 - \mathbf{r}_b|/|\mathbf{r}_1 - \mathbf{r}_2|$, with $\mathbf{r}_1$ being the fluid node at which the fluid particles originate and $\mathbf{r}_2 = \mathbf{r}_1$

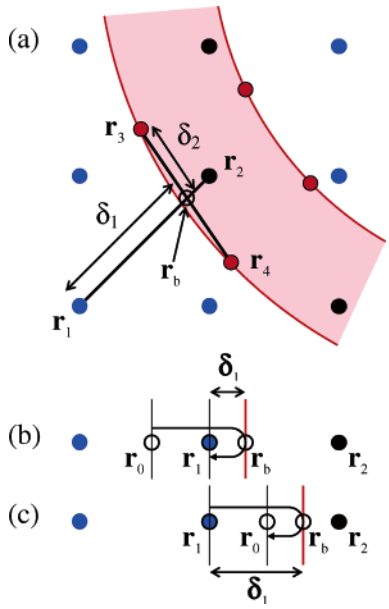

Figure 2. Implementation of solid−fluid boundary conditions (see text for details).

$+ \mathbf{c}_i\Delta t$ being the neighboring solid node in the direction of the fluid particles' motion. For $\delta_1 = 1/2$, these particles will arrive back at node $\mathbf{r}_1$ after precisely one time step with a velocity that is opposite in direction to their original motion. This situation represents the well-known link bounce-back rule.[13] However, for $\delta_1 \neq 1/2$, fluid particles will end up at positions that do not coincide with a regular lattice node, and some sort of interpolation is needed. We follow the scheme that is developed by Bouzidi et al. and described in detail in ref 30.

First we consider the case of a stationary interface. For $\delta_1 < 1/2$, we obtain $f_i^*(\mathbf{r}_0,t)$, the postcollision distribution at the position $\mathbf{r}_0$, by linear interpolation between $f_i^*(\mathbf{r}_1 - \mathbf{c}_i\Delta t,t)$ and $f_i^*(\mathbf{r}_1,t)$ (see Figure 2b). After traveling for one time step and being reflected at the boundary node, the interpolated postcollision distribution at $\mathbf{r}_0$ will end up precisely at node $\mathbf{r}_1$ with a velocity in the opposite direction (see Figure 2b). Hence[30]

$$f_k(\mathbf{r}_1,t+\Delta t) = f_i^*(\mathbf{r}_0,t) = (1-2\delta_1)f_i^*(\mathbf{r}_1 - \mathbf{c}_i\Delta t,t) + 2\delta_1 f_i^*(\mathbf{r}_1,t), \quad \delta_1 < \frac{1}{2} \tag{5}$$

Here, the subscript k stands for fluid particles with a velocity in the opposite direction of the incoming particles, i.e., $\mathbf{c}_k = -\mathbf{c}_i$. For $\delta_1 \geq 1/2$, we propagate the fluid particles at node $\mathbf{r}_1$, such that they end up at the position $\mathbf{r}_0$, i.e., $f_k(\mathbf{r}_0,t+\Delta t) = f_i^*(\mathbf{r}_1,t)$ (see Figure 2c). We then obtain $f_k(\mathbf{r}_1,t+\Delta t)$ by linear interpolation between $f_k(\mathbf{r}_1 - \mathbf{c}_i\Delta t,t+\Delta t)$ and $f_k(\mathbf{r}_0,t+\Delta t)$, i.e.[30]

$$f_k(\mathbf{r}_1,t+\Delta t) = \frac{2\delta_1 - 1}{2\delta_1} f_k(\mathbf{r}_1 - \mathbf{c}_i\Delta t,t+\Delta t) + \frac{1}{2\delta_1} f_k(\mathbf{r}_0,t+\Delta t) = \frac{2\delta_1 - 1}{2\delta_1} f_k^*(\mathbf{r}_1,t) + \frac{1}{2\delta_1} f_i^*(\mathbf{r}_1,t), \quad \delta_1 \geq \frac{1}{2} \tag{6}$$

For a moving interface, we have to account for the velocity $\mathbf{u}_b$ of the solid material at the intersection point $\mathbf{r}_b$. This leads to additional terms in eqs 5 and 6 that are proportional to the component of the velocity $\mathbf{u}_b$ in the direction of the fluid particle's velocity[30]

$$f_k(\mathbf{r}_1,t+\Delta t) = (1-2\delta_1)f_i^*(\mathbf{r}_1 - \mathbf{c}_i\Delta t,t) + 2\delta_1 f_i^*(\mathbf{r}_1,t) - \frac{2\alpha_i}{c_f^2}\rho(\mathbf{r}_1,t)\mathbf{c}_i\cdot\mathbf{u}_b(\mathbf{r}_b,t), \quad \delta_1 < \frac{1}{2} \tag{7a}$$

$$f_k(\mathbf{r}_1,t+\Delta t) = \frac{2\delta_1 - 1}{2\delta_1} f_k^*(\mathbf{r}_1,t) + \frac{1}{2\delta_1} f_i^*(\mathbf{r}_1,t) - \frac{\alpha_i}{\delta_1 c_f^2}\rho(\mathbf{r}_1,t)\mathbf{c}_i\cdot\mathbf{u}_b(\mathbf{r}_b,t), \quad \delta_1 \geq \frac{1}{2} \tag{7b}$$

Here, $\alpha_i = 1/3$ for the orthogonal directions and 1/12 for the diagonal links. The velocity $\mathbf{u}_b$ is obtained through a straightforward interpolation between the velocities of the lattice spring nodes on either side of the intersection point, i.e., $\mathbf{u}_b(\mathbf{r}_b,t) = (1-\delta_2)\mathbf{u}(\mathbf{r}_3,t) + \delta_2\mathbf{u}(\mathbf{r}_4,t)$, with $\delta_2 = |\mathbf{r}_3 - \mathbf{r}_b|/|\mathbf{r}_3 - \mathbf{r}_4|$ (see Figure 2a). This implementation gives a no-slip boundary condition at the solid−fluid interface, with errors that are of second-order accuracy in the spatial discretization.[30]

As a result of the bounce-back process, the fluid exerts a force on the solid−fluid interface. This force is taken to be equal to the rate of exchange in momentum that takes place as the fluid particles are reflected at the interface, i.e.

$$\mathbf{F}_b\left(\mathbf{r}_b,t+\frac{1}{2}\Delta t\right) = \{[f_i^*(\mathbf{r}_1,t) - \alpha_i\rho(\mathbf{r}_1,t)]\mathbf{c}_i - [f_k(\mathbf{r}_1,t+\Delta t) - \alpha_i\rho(\mathbf{r}_1,t)]\mathbf{c}_k\}\frac{\Delta x^2\Delta x_{LS}}{\Delta t} \tag{8}$$

Here, the terms $\alpha_i\rho(\mathbf{r}_1,t)$ compensate for the ambient pressure, ensuring that the force on the interface is zero when the entire system is at rest.[15] $\mathbf{F}_b$ is then distributed to the lattice spring nodes on either side of the intersection point, while conserving the normal and tangential force on the interface:

$$\mathbf{F}_b\left(\mathbf{r}_3,t+\frac{1}{2}\Delta t\right) = (1-\delta_2)\mathbf{F}_b\left(\mathbf{r}_b,t+\frac{1}{2}\Delta t\right) \tag{9a}$$

$$\mathbf{F}_b\left(\mathbf{r}_4,t+\frac{1}{2}\Delta t\right) = \delta_2\mathbf{F}_b\left(\mathbf{r}_b,t+\frac{1}{2}\Delta t\right) \tag{9b}$$

Validation. We test the properties of our cylindrically symmetric LSM shell by simulating the "breathing modes" of an empty shell in a vacuum and comparing the results with theory.[31] After an initially uniform radial expansion, the shell contracts and expands periodically ("breaths") with a characteristic frequency. We find the relative error in this so-called breathing mode frequency to decrease as N^{-2} independent of material properties; that is, if the number of nodes is doubled, then the accuracy increases 4-fold. Hence, the lattice spring model is indeed of second-order accuracy in the spatial resolution. In particular, we find the error to be smaller than 1% for $N = 40$ and $n = 3$.

We verify the boundary rules for a static noncompliant interface by simulating the drag force on a regular array of parallel cylinders, whose axes lie perpendicular to the mean flow direction. This problem can be simulated in two dimensions by placing a single disk in a square box with periodic boundary conditions applied in both directions. Here, a single layer of lattice spring

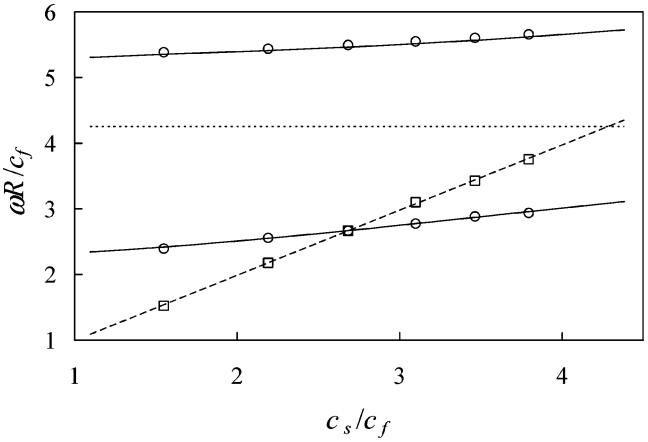

Figure 3. Dimensionless breathing-mode frequency as a function of the ratio between the speeds of sound in the solid, c_s, and the fluid, c_f. Here, c_f is fixed and c_s is varied by changing the Young's modulus of the shell. Simulation results for empty shells in vacuo (□) and for fluid-filled shells in vacuo (○) are compared with the theoretical predictions (the solid lines and dashed line, respectively). The dotted line represents the lowest order breathing-mode frequency for a fluid in a rigid shell.

nodes, whose positions are fixed in space, represents the outer surface of the cylinder. The center of the cylinder is placed in the center of a box with dimensions $L = 101$. The volume fraction $\varphi = \pi R^2/L^2$ is varied by varying the cylinders radius $R = N\Delta x_{LS}/2\pi$, while fixing $N = 60$. In addition, the respective fluid density and shear viscosity are given by $\rho_f = 1$ and $\mu = 1/6$. The flow around the cylinder is driven by a constant pressure gradient. The total drag force on the cylinder is calculated by integrating the boundary force, obtained from eqs 8 and 9, over the entire surface. This value is compared with the theoretical prediction for the drag force on a periodic array of cylinders.[32] The relative error in our result ranged from 0.4% for $\varphi = 0.05$ to 2.1% for $\varphi = 0.6$. Increasing N to 180 resulted in relative errors ranging from 0.2% for $\varphi = 0.05$ to 0.6% for $\varphi = 0.6$.

Next, we validate the coupled LBM/LSM model in two dimensions by simulating the breathing modes of a fluid-filled cylindrical shell in a vacuum. Here, we fix the density and the shear viscosity of the encapsulated fluid to $\rho_f = 1$ and $\mu = 1/6$, respectively, as well as the density of the shell $\rho_s = 3/2$. The shell is represented by three layers of $N = 120$ lattice spring nodes and has an outer radius $R = 50$; hence, $\Delta x_{LS} = 2\pi R/(\pi + N) \approx 2.5$. We then vary the Young's modulus of the shell, E_c. After the system has undergone an initially uniform radial expansion, we determine the frequency spectrum of the oscillations as a function of the ratio c_s/c_f. Here, $c_f = 1/\sqrt{3}$ is the speed of sound in the fluid. The results are shown in Figure 3, where the frequencies are nondimensionalized with the outside radius of the shell and the speed of sound in the fluid. The spectrum is obtained through a Fourier analysis of the averaged radial displacement vs time. The solid lines are the theoretical predictions for an inviscid fluid. Although our fluid has a finite viscosity, we remain in the weak-damping region, where the influence of the viscosity on the frequencies is negligibly small. In Figure 3, we also plot the breathing mode frequency of an empty shell for the same range of parameters. The results indicate that our coupled model captures the correct frequencies to within 1% of the theoretical prediction for a large range of c_s/c_f.

Finally, we study the effect of the spatial resolution of the lattice on the breathing mode frequencies of a fluid-filled cylindrical shell in a vacuum. We use the same fluid and solid properties as in the example above but vary the outside radius of the shell. First, we vary Δx_{LS}, while keeping the ratio h/R fixed. Here, we use $N = 120$, $n = 3$ and set the shell's Young's modulus to $E_c = 1$ or, equivalently, $c_s/c_f = (2/5)\sqrt{15}$. The frequency of the lowest mode is found to match the theoretical prediction to within the accuracy of our analysis (±0.3%) for $25 \le R \le 50$. The relative error in the frequency of the second mode is 2.2% for $R = 25$ and decreases as R^{-2}. Second, we vary N and n, while keeping $\Delta x_{LS} = 25\pi/(60 + \pi)$ and $h/R = 2\pi/(60 + \pi)$ fixed. The relative error of the first mode is less than 0.3% for $12.5 \le R \le 50$, while that in the second mode is 3.7% at $R = 12.5$, again decreasing as R^{-2}. Hence, the accuracy of the coupled system is of the second order in the spatial resolution of the lattice; this level of accuracy is the same as that of the underlying lattice spring model (as shown above) and lattice Boltzmann model.[13] This illustrates that our new implementation of the boundary conditions at the solid−fluid interface is indeed of second-order accuracy in the spatial resolution.

Results and Discussion

In what follows, we describe our investigations into the roles that surface compliance and topography play in the motion of microcapsules that pass over the substrates. The top wall of our simulation box is flat and noncompliant; it moves with a constant velocity U_{wall}, and its sole function is to drive the flow. The bottom wall is stationary and serves as our substrate. Periodic boundary conditions are applied in the flow direction (the x direction). We study capsule motion past flat, uniform substrates, past a substrate with periodic variations in its stiffness, and past topographically patterned substrates. In each case, the length of the simulation box in the flow direction is $L_x = 500$, while the height between the top of the substrate and the moving wall is $L_y = 75$.

We focus on a single capsule that interacts with the substrate through a Morse potential

$$\phi(r) = \epsilon\left(1 - \exp\left[-\frac{(r - r_0)}{\kappa}\right]\right)^2 \qquad (7)$$

where ϵ and κ characterize the respective strength and range of the interaction potential, r is the distance between a pair of LSM nodes, where one node lies on the shell's outer surface and the other lies at the substrate−fluid interface, and r_0 is that distance between the capsule and the substrate where the force is equal to zero.

In terms of dimensionless numbers, we can characterize the motion of a capsule along a substrate by the Reynolds number $\mathrm{Re} = \rho\gamma R^2/\mu$ and the capillary number $\mathrm{Ca} = \gamma\mu R/E_c h$. Here, $\gamma = U_{wall}/L_y$ is the applied shear rate, ρ and μ are the respective density and shear viscosity of the host fluid, R is the outside radius of the undeformed capsule, E_c is the Young's modulus of the capsule's shell, and h is its thickness. The Reynolds number characterizes the relative importance of inertial and viscous effects. The capillary number represents the relative importance of the viscous stress in the surrounding fluid and elastic stress in the capsule's shell. To relate our simulations to actual experimental condi-

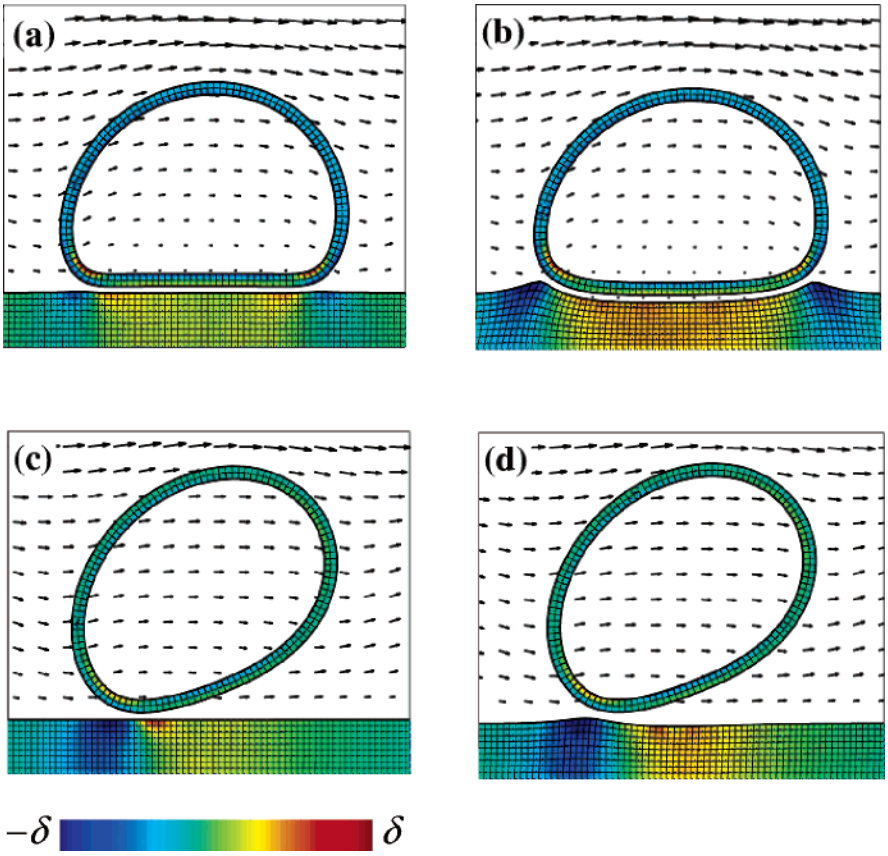

Figure 4. Capsule rolling on a flat uniform substrate for Ca = 8×10^{-4} and varying stiffness and interaction strength: (a) $E = 1$, $\Phi = 1.15$; (b) $E = 0.03$, $\Phi = 1.15$; (c) $E = 1$, $\Phi = 0.12$; (d) $E = 0.03$, $\Phi = 0.12$. The color indicates the local strain: $\delta = 0.05$ for the capsule shell, while for the substrate $\delta = 0.02$, 0.2, 0.002, and 0.05 for (a), (b), (c), and (d), respectively.

tions, we compare the Reynolds and capillary numbers in our simulations to those for a leukocyte rolling in a blood vessel under physiological conditions. For leukocytes with radii of the order of 5 μm in an aqueous solution, typical values are Re $\sim 10^{-2}-10^{-3}$ and Ca $\sim 10^{-3}-10^{-4}$.[16,18] The fact that Re $\ll 1$ implies that inertia has a negligible effect on the leukocyte dynamics compared to the viscous forces.[33] Although such a small Reynolds number is well within reach of the lattice Boltzmann method, we can speed up our calculations considerably by using a larger Re. Hence, we set the shear rate such that Re ~ 0.1, which is still sufficiently small that inertial effects in the fluid can be neglected. The other parameters are chosen so that Ca $\sim 10^{-3}-10^{-4}$; in this manner, the deformation of the capsule due to the shear flow is comparable to that experienced by rolling leukocytes. Note that a more detailed comparison between simulation parameters and experimental values is given in the last subsection.

In the course of our study, we vary Ca by systematically altering γ; the other parameters in the definitions of Ca are fixed at constant values in all our simulations. We use $\rho_f = 1$ and $\mu = 1/6$ for both the host and the encapsulated fluids. For the capsule's shell, we use $R = 25$, $E_c = 5/12$, $N = 120$, and $n = 3$, giving $\Delta x_{LS} = 25\pi/(60 + \pi) \approx 1.24$ and $h = 2\Delta x_{LS} \approx 2.5$. Furthermore, we fix $\rho_s = 3/2$, resulting in a speed of sound in the shell of $c_s = 1/\sqrt{3}$ (which is equal to the speed of sound in the fluids). We set $\kappa = 1$ and $r_0 = 1.8$ in all our simulations. When applied to a capsule whose radius is 5 μm, this choice in r_0 yields a distance of 0.36 μm between the capsule and the surface. For a leukocyte whose radius is roughly 5 μm, the latter distance does in fact correspond to the length of the microvilli[18] ($\sim 0.3-0.4$ μm), which separates the cell and the endothelial layer.

We also introduce a dimensionless interaction strength $\Phi = \epsilon N/E_c h \kappa^2$ (see eq 7), representing the ratio of the interaction strength to the membrane stiffness. For $\Phi \gg 1$, this interaction leads to significant deformation of the capsule, while for $\Phi \ll 1$, the effect on its shape is small. The Young's modulus of the substrate, E_s, is expressed in terms of the dimensionless number $E = E_s/E_c$. (Recall that E_c is held constant throughout.) In what follows, all lengths, velocities, and forces are nondimensionalized by dividing these quantities by R, γR, and $\mu\gamma R^2$, respectively.

Planar Substrate. Before considering the case of the mechanically and topographically heterogeneous surfaces, we first examine the motion of the capsules on a mechanically uniform, flat substrate. By varying the spring constants in the LSM lattice for the substrate, we can systematically modify the stiffness of this surface. We can then investigate how the capsule's movement due to the imposed flow is affected by variations in E and Φ.

Figure 4 shows snapshots of the capsule's motion along a uniform, flat surface. Here, the substrate comprises 10 layers of lattice spring nodes. The colors in the images indicate the relative strain within the substrate and capsule's shell; the color bar indicates the range of the deformation, with positive values indicating an expansion of the springs and negative values a contraction. For sufficiently high values of the interaction strength Φ, the capsules remain localized on the substrate and undergo a rolling motion. The observation of capsule rolling is in agreement with experimental

studies of leukocytes moving on the endothelial surface of blood vessels.[34]

For the relatively high value of $\Phi = 1.15$, the contrast between a capsule rolling on a stiff vs a fairly compliant surface can clearly be seen by comparing parts a and b of Figure 4. In both cases, the lower part of the capsule aligns with the substrate due to the strong adhesive interaction. For $E = 1$, the substrate is nearly flat and effectively rigid (Figure 4a). In the case of the more compliant layer (Figure 4b, for $E = 0.03$), the surface forms a "crater" underneath the capsule. The material directly underneath the capsule is compressed, whereas the material forming the edge of the crater is stretched. For this high value of Φ, the capsule's shape is predominantly determined by the interaction with the substrate. Hence, although the drag force slightly skews the capsule, the effect is small and the capsule's shape remains nearly symmetric in the flow direction. The incompressible nature of the encapsulated fluid prevents the capsule from collapsing. Note that the deformation of the shell gives rise to an increase in the pressure within the encapsulated fluid, as is reflected in an overall increase in strain within the shell (see Figure 4).

Figure 4c,d shows snapshots of the capsules on the same substrates as in Figure 4a,b, but now the interaction strength, $\Phi = 0.12$, is relatively weak. For such a weak attraction, the capsule's shape is mostly defined by the hydrodynamic interaction between the capsule and the surrounding host fluid. The shear flow tends to elongate the capsule and align it in a direction that is inclined with respect to the flow direction. Note that even for this small value of Φ, the compliant nature of the wall leads to a visible elevation of the substrate underneath the capsule that gradually disappears for stiffer surfaces (compare parts c and d of Figure 4). This elevation is due to a combination of the surface attraction and the lift force acting on a capsule in the shear flow. Relative to the capsules on the stiff substrate (Figure 4a,c), for soft substrates, the contact area between the capsule and substrate is increased for large interaction strength (Figure 4b) and somewhat decreased for weak attraction (Figure 4d).

Figure 4 clearly shows that the shape of the capsule is affected by both the stiffness of the substrate and the strength of the capsule−substrate interaction.These factors will also influence the capsule's motion along the substrate. We first discuss the capsule dynamics on a relatively stiff surface. To quantify this behavior, we define the dimensionless rolling velocity, U, as the capsule's center of mass velocity parallel to the substrate normalized by γR. In Figure 5a, we plot U as a function of Φ for $E = 1$ and different values of Ca. The plot shows that the dimensionless rolling velocity depends predominantly on the interaction strength and that it decreases with increasing Φ for all values of Ca. For $\Phi > 0.5$, U is virtually independent of Ca. Here, the capsule is compressed due to its attraction to the substrate (see Figure 4a), and its shape is almost completely determined by the interaction with the substrate. Because of the scaling with γR (through the normalization of U), the rolling velocity is directly proportional to the applied shear rate.

Increasing the interaction strength reduces the capsule's cross section in the flow direction (Figure 4a), and consequently, its rolling velocity since the viscous drag is proportional to the capsule's cross section. For small

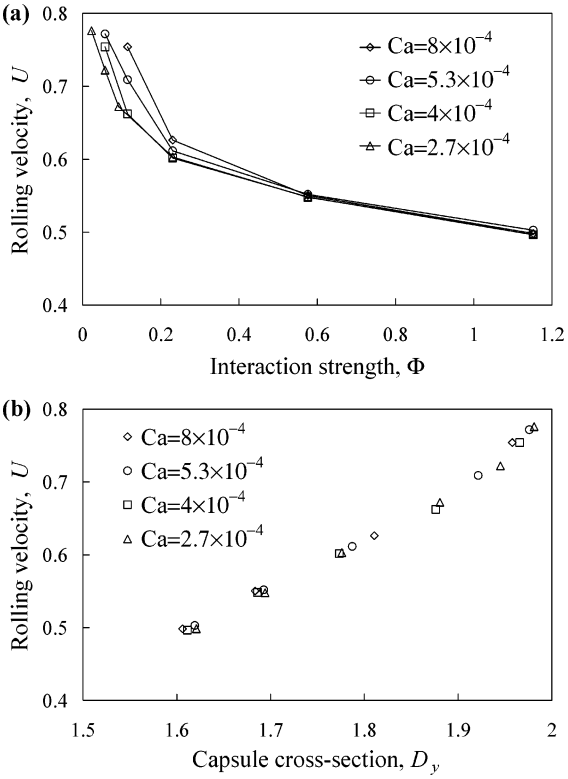

Figure 5. Rolling velocity of the capsule on the stiff substrate with $E = 1$ as a function of the interaction strength Φ (a) and the capsule's cross section in the y direction D_y (b) for different values of Ca.

values of Φ, the capsule's shape is elongated by the flow field and inclined with respect to the flow direction (Figure 4c). This increases the capsule's cross section and hence enhances its rolling velocity. The increase in U with decreasing Φ is slightly more pronounced for large values of Ca, for which the capsule experiences greater deformation by the shear flow. These results suggest that for a relatively stiff substrate the rolling velocity is not directly affected by the interaction potential, but rather, indirectly through the dependence of the capsule's shape on Ca and Φ. To confirm this notion, in Figure 5b we plot the data from Figure 5a as a function of the capsule's cross section in the flow direction, D_y (nondimensionalized with R). For all the values of Ca and Φ, these results clearly show a direct correlation between the capsule's cross section and its rolling velocity relative to γR.

To obtain more insight into the factors that affect the capsule dynamics, we analyze the behavior of rolling velocity U, the capsule's cross section in the flow direction, D_y (normalized by R), and the x-component of the force that the substrate exerts on the capsule, F_x, over the range of E considered here ($0.01 \leq E \leq 1$). The plots in Figure 6 contain curves for different values of Φ, and the data are for the relatively high value of $\mathrm{Ca} = 8 \times 10^{-4}$.

For relatively stiff substrates ($0.1 < E \leq 1$), the rolling velocity and shape of the capsule are nearly independent of E (Figure 6a,b), suggesting that we can effectively consider these substrates to be rigid. Figure 6c shows that $F_x \approx 0$ for these stiff substrates. The plots reinforce our discussion of Figure 5 since they indicate that the capsule's rolling velocity is fully determined by the drag force due to the applied shear flow. For $0.1 < E \leq 1$, Figure 6a,b further shows that the decrease in the

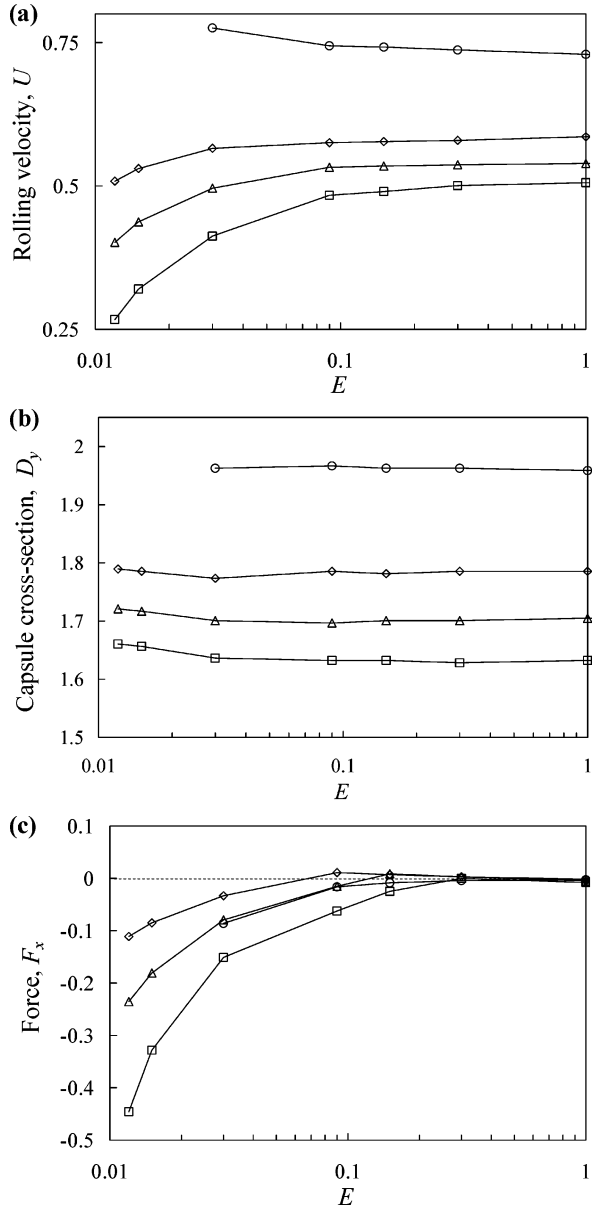

Figure 6. (a) Rolling velocity, (b) capsule cross section, and (c) x-component of the force exerted on the capsule by the substrate vs substrate stiffness for Ca = 8×10^{-4} and different interaction strengths: (□) $\Phi = 1.15$, (△) $\Phi = 0.58$, (◇) $\Phi = 0.23$, (○) $\Phi = 0.12$.

rolling velocity with increasing Φ is due to a decrease in the capsule's cross section in the flow direction.

For relatively compliant substrates ($0.01 \leq E < 0.1$), Figure 6a shows that there is a significant impact of E on the capsule's rolling velocity. Furthermore, the net result is qualitatively different for large and small interaction strengths. For large values of Φ, we see a decrease of U with decreasing E (Figure 6a). However, this decrease cannot be attributed to variations in the capsule's cross section, which is nearly independent of E for a given value of Φ (Figure 6b). Instead, Figure 6c indicates that the decrease of U with decreasing E is caused by the appearance of a net force that is exerted by the substrate on the capsule in the direction opposite to the flow direction. This force arises from the deformation of the surface as the capsule "plows" its way through the surface (see Figure 4b) (as opposed to rolling on top of the substrate, as is the case for a rigid surface (see Figure 4a)). In addition, the force becomes larger for softer substrates. In this scenario, energy is transferred from the capsule to the surface through the excitation of vibrations in the substrate. Although the substrate itself is elastic and, hence, cannot dissipate energy, the vibrational energy is transmitted back to the fluid at the fluid−substrate interface, where it is subsequently dissipated.

For small values of Φ, decreasing E leads to a slight increase in the rolling velocity (Figure 6a for $\Phi = 0.12$). Here, the combination of the lift force and the attractive potential causes an elevation of the substrate under the capsule (Figure 4d), reducing the contact area between the capsule and the substrate and moving the capsule away from the substrate toward a region of higher fluid velocity. This contributes to an increase in the rolling velocity. A further decrease in E increases the surface elevation of the substrate under the capsule, leading to a further decrease in the area of contact and thus promoting detachment of the capsule from the substrate.[35] In particular, for $\Phi = 0.06$, detachment occurs for any ratio E, while for $\Phi = 0.12$, detachment occurs only for $E < 0.02$.

Mechanically Patterned Surface. The results for the uniform substrates show that the compliance of the surface greatly affects the capsule's motion. Observing that the capsules move differently on hard and soft surfaces, we hypothesize that mechanically patterned surfaces, i.e., substrates that encompass periodic variations in stiffness, could be harnessed to control the capsule's dynamic behavior. To test this hypothesis and optimize the design of effective surfaces, we examine substrates with alternating stiff and flexible regions of equal length $P/2$, with P being the period of the overall pattern normalized by R. Such mechanically patterned surfaces, which exhibit well-defined micron-scale features, can readily be fabricated with modern microfabrication techniques.[19] In our study, we set $E = 1$ for the hard domains and $E = 4 \times 10^{-3}$ for the soft areas of the substrate. The Young's modulus of the stiff areas is sufficiently high that these regions can be viewed as flat, rigid domains. We fix Φ at 0.58, which is sufficiently large that the capsule remains bound to the surface. We then systematically vary the capillary number Ca and the period P. Quite remarkably, we find that as a function of these parameters the capsule either stops at a specific location on the surface or keeps traveling along the substrate.

Figure 7a,b shows the final structures for two cases where the capsule comes to a standstill, while Figure 7c shows a snapshot for a case where the capsule keeps moving along the surface. When a capsule stops, it always does so at the end of a soft domain, where a small bump appears on the surface. (Note that the neighboring stiff region remains nearly flat.) The material in this bump is seen to undergo significant strain. As shown in Figure 8a, this deformation results in a net force in the direction opposite to the imposed flow; for sufficiently low shear rates, this force balances the hydrodynamic drag. Although the capsule no longer moves along the substrate, it keeps rotating due to the applied shear flow.

Our observations are summarized in Figure 9, where we plot a "phase map", indicating whether a capsule will stop or continue moving as a function of the capillary number Ca and substrate period P. Here, the crosses indicate situations where the capsule's motion is arrested, while the solid circles mark parameters for

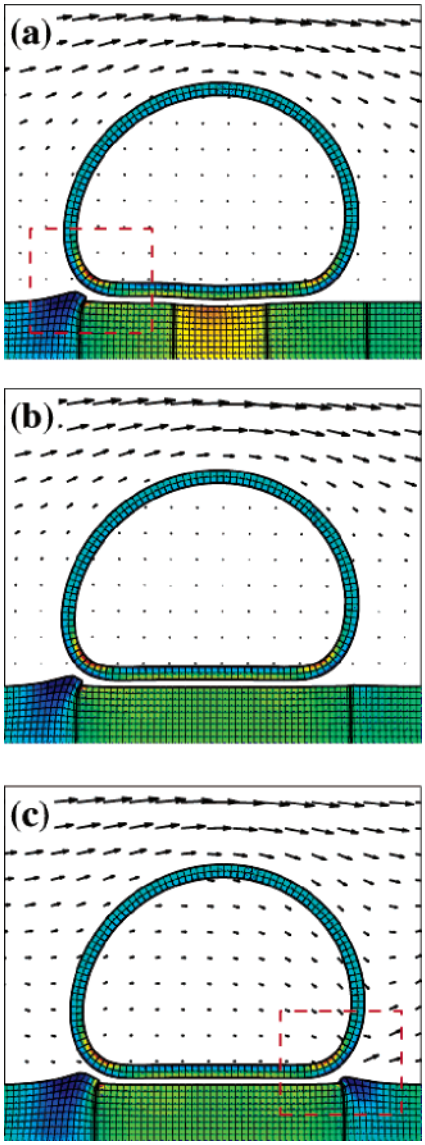

Figure 7. Snapshots of capsules on mechanically patterned substrates for Ca = 2.7×10^{-4} and $\Phi = 0.58$: (a) $P = 1.44$; (b) $P = 4.32$; (c) $P = 3.84$. (a) and (b) show situations where the capsule stops, while in (c) it keeps rolling. When a capsule stops (a and b), it always does so at the end of a soft domain, where a small bump appears on the surface. This deformation results in a net force in the direction opposite to the imposed flow (Figure 8a); for sufficiently low shear rates, this force balances the hydrodynamic drag. For $P = 3.84$ (c), the contact area between the capsule and the substrate is roughly equal to $P/2$. Every time the receding portion of this capsule reaches the end of a soft patch, the leading edge lies in contact with the next soft patch. For this case, the forces acting on both sides of the capsule are roughly equal in magnitude and opposite in sign (see Figure 8a,b), thus canceling their effect and allowing the capsule to continue rolling. The colors are as in Figure 4 with $\delta = 0.05$ and 0.1 for the capsule shell and the substrate, respectively. The dashed boxes in (a) and (c) indicate the closeup areas presented in (a) and (b) of Figure 8, respectively.

which the motion is unimpeded. As can be seen, the capsules stop for any P when Ca $\leq 1.6 \times 10^{-4}$, while they roll for any P for Ca $\geq 3.7 \times 10^{-4}$. In between these limiting values, the capsules can either roll or stop depending on the substrate period. Note that for a given P a small increase in the capillary number will release a previously stationary capsule. Since Ca $= \gamma\mu R/E_c h$,

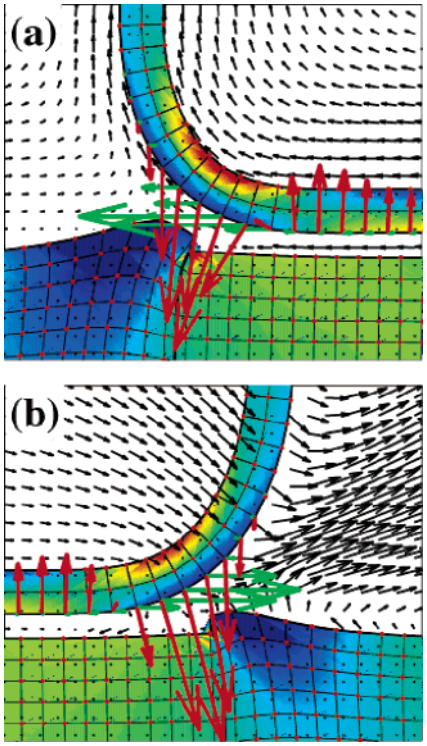

Figure 8. Closeups (a) and (b) show the detailed flow fields and the interaction forces of (a) and (c) of Figure 7, respectively. The x-component of the force is magnified 3-fold for clarity.

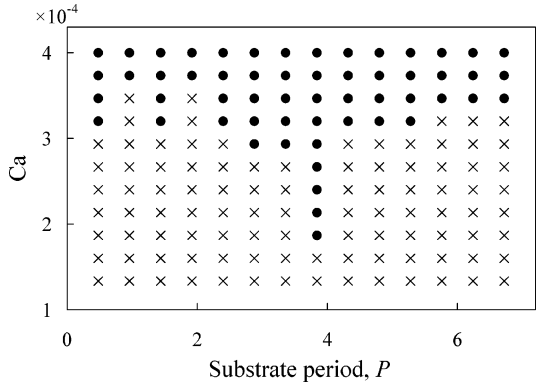

Figure 9. Summary of the capsule behavior for varying Ca and P and a fixed interaction strength $\Phi = 0.58$. The crosses are for situations where the capsule stops, while the circles indicate parameters for which it keeps rolling.

this increase can most easily be obtained by an increase in the shear rate γ.

Thus, the mechanically patterned surfaces provide a means of regulating the trafficking of the capsules on the substrate. In particular, the surface can be utilized to halt the capsules at a particular location, where they can undergo further analysis or processing; by increasing γ, the capsules can subsequently be made to continue traveling through the system.

We note that there is a special value $P \approx 3.8$ for which the capsule keeps rolling along the substrate even for very low values of Ca. In this case, the contact area between the capsule and the substrate is roughly equal to $P/2$. Every time the receding portion of this capsule reaches the end of a soft patch (where it would be expected to stop (Figure 7a,b)), the leading edge lies in contact with the next soft patch (Figure 7c). For this case, the forces acting on both sides of the capsule are

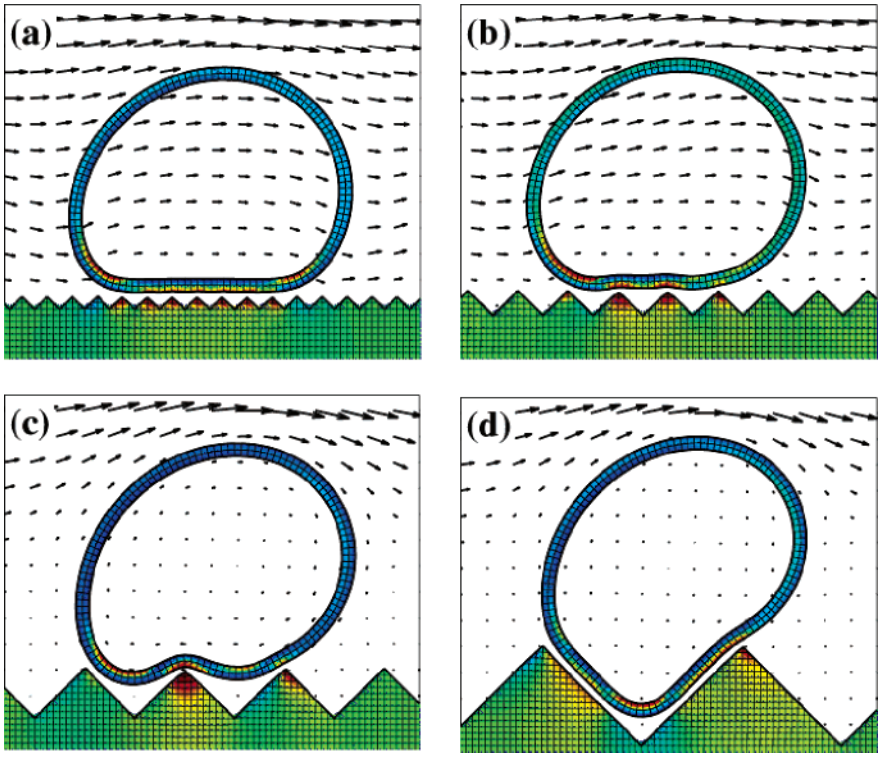

Figure 10. Snapshots of capsules on corrugated substrates for Ca = 5.3×10^{-4}, $E = 1$, and $\Phi = 0.58$: (a) $P = 0.192$; (b) $P = 0.384$; (c) $P = 0.768$; (d) $P = 1.536$. (a) and (b) show situations where the capsules keep rolling, while in (c) and (d) they stop. The colors are as in Figure 4 with $\delta = 0.02$ for both the capsule shell and the substrate.

roughly equal in magnitude and opposite in sign (see Figure 8a,b), thus canceling their effect and allowing the capsule to continue rolling.

When the capsule rolls along the patterned substrate, its velocity varies with time. However, its average velocity $\langle U \rangle$ was found to be nearly independent of P and roughly the same as the value found for a uniform substrate with a Young's modulus equal to that of the soft areas.

Corrugated Substrate. Because of advances in soft lithography, researchers can fabricate not only mechanically patterned surfaces but also topographically patterned substrates such as regular saw tooth patterns[36] or regular arrays of compliant posts.[19] Inspired by recent studies on the effect of surface roughness on the motion of fluid droplets,[37] we first examine how uniform corrugation of the substrate affects the capsule's motion along the substrate. Such a corrugated surface can be regarded as a simple model for substrate roughness. In the next section, we discuss the effect of compliant posts.

In Figures 10 and 11, we present snapshots of capsules that are moving on corrugated substrates for different interaction strengths. Here, we focus on the case of $E = 1$, where the Young's moduli for the substrate and the capsules are the same. We also fix the capillary number at Ca = 5.3×10^{-4}. Here, the period P is taken to be the distance between the peaks, and the height of the peaks is equal to $P/2$. Recall that P is in units of R, the radius of the undeformed capsule. Figures 10 and 11 show that the capsule shape and motion are greatly affected by both the interaction strength and the period P.

For $P \ll 1$, the capsule is in contact with multiple peaks and the lower part of this capsule remains nearly flat. Although the interaction strength affects the size of the contact area, the capsule's motion is qualitatively similar for different values of Φ (as long as Φ is sufficiently large to keep the capsules adhered to the substrate). The capsule rolls smoothly along the substrate in a manner that is very similar to its rolling on a flat homogeneous substrate (compare Figures 10a and 11a with Figure 4a). When P is increased, the motion becomes qualitatively different for small and large values of Φ. For the relatively large value of $\Phi = 0.58$, the lower part of the shell becomes significantly deformed by the interaction with the substrate, as it tries to accommodate to the shape of the grooves. This deformation becomes more pronounced for increasing P (Figure 10b–d). For smaller values of Φ, the capsule keeps rolling on the tips of the asperities (see Figure 11). In this case, its shape is hardly affected by the value of P. Moreover, the shell remains convex in contrast to that for the stronger interaction (compare Figure 10b–d to Figure 11b–d). Because of the shear flow, the capsule becomes slightly elongated and inclined with respect to the flow direction, much like that for a flat substrate (compare Figure 11b–d with Figure 4c).

In Figure 12, we summarize the average rolling velocity, $\langle U \rangle$, normalized with γR as before, vs the period P for a range of Φ. Here, $P = 0$ corresponds to a flat, homogeneous substrate. As seen in Figure 12 for $\Phi \geq 0.58$, the strong adhesion reduces the rolling velocity (see also Figure 10b) and eventually causes the capsule to stop for larger values of P (Figure 10c,d). At even higher P, the capsule can move continuously on the substrate if the surface attraction is not too strong (see Figure 12 for $\Phi = 0.58$ and $P \approx 1.8$). In this case, the capsule is able to move along a trajectory that follows the surface topography.

When the interaction strength is ~0.23 or less, the dynamical behavior of the capsule changes quite significantly. Here, the capsule travels along the substrate for any value of P (Figure 12). In particular, it keeps "floating" slightly above the tips of the asperities, unless

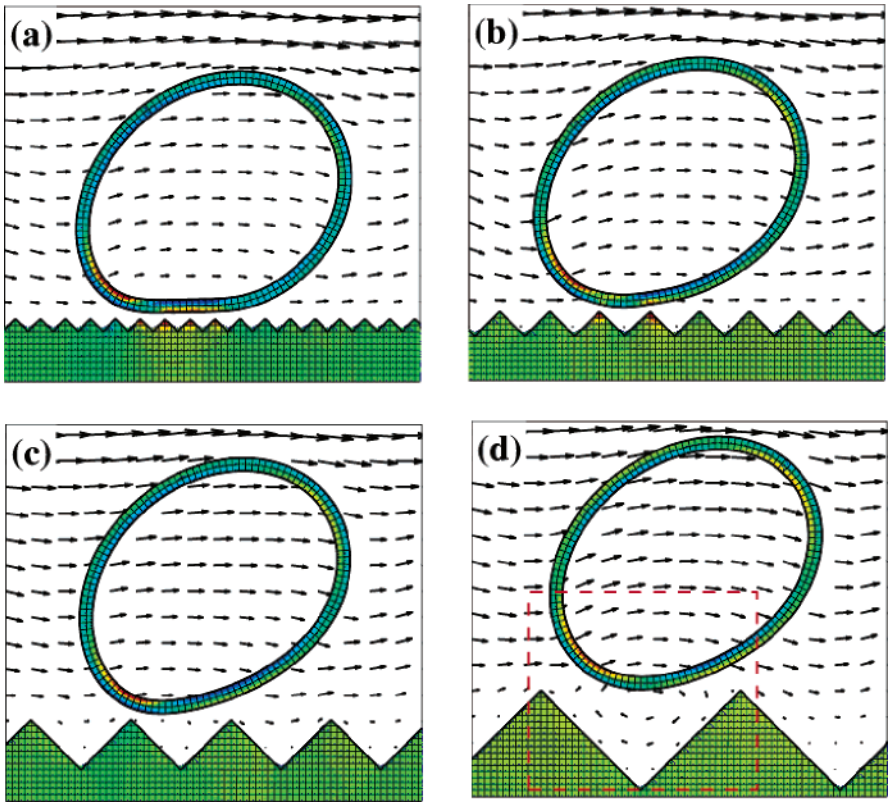

Figure 11. Snapshots of capsules on corrugated substrates for Ca = 5.3×10^{-4}, $E = 1$ and $\Phi = 0.23$: (a) $P = 0.192$; (b) $P = 0.384$; (c) $P = 0.768$; (d) $P = 1.536$. In all the snapshots the capsules keep rolling. The colors are as in Figure 4 with $\delta = 0.02$ for both the capsule shell and the substrate. The dashed box in (d) indicates the closeup area that is presented in Figure 13.

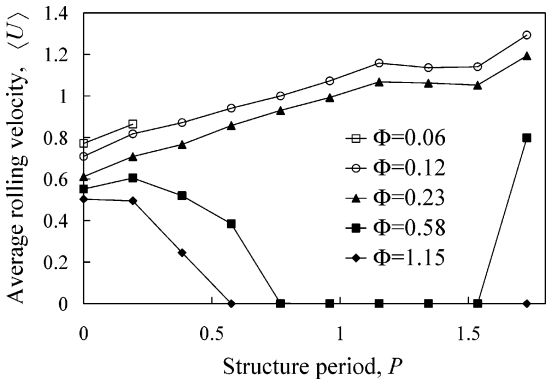

Figure 12. Average rolling velocity of a capsule moving along a corrugated substrate vs the pattern period for varying interaction strength Φ. Here, Ca = 5.3×10^{-4} and $E = 1$.

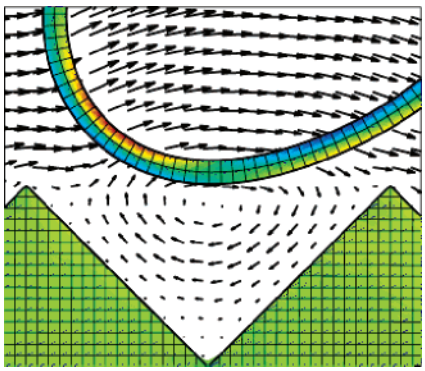

Figure 13. Closeup of the detailed flow field in Figure 11d.

the interaction strength is too weak, whereupon the capsule completely detaches from the surface (see Figure 12 for $\Phi = 0.06$). As the capsule travels above the valley of a groove, a vortex appears within the groove, as shown in Figure 13. It appears that this vortex contributes to the prevention of capsule detachment, as it creates a "suction" force when the capsule approaches the next ridge. Note that in the course of the "floating" motion the rolling velocity varies slightly with time. However, the amplitude of the variations does not exceed 10% of the average rolling velocity. The capsule also exhibits small periodic oscillations in the shape and vertical position.

Figure 12 indicates that in the "floating" regime ($\Phi \leq 0.23$) there exists a large range of P for which the average rolling velocity increases almost linearly with P. Figure 14 shows that this is actually the case for a much wider range of flow conditions. Here, the average rolling velocity is plotted as a function of the substrate period for different values of Ca and Φ, normalized by the rolling velocity for a similar capsule on a flat uniform, substrate with $E = 1$. First, we note that the rolling velocity past a corrugated substrate is significantly higher than that for rolling past an otherwise comparable flat substrate (up to about a 2-fold increase at $P \approx 1.8$). More importantly, however, one can see that in all these cases the rolling velocity follows the same trend and scales essentially linearly with P for a large range of P.

From the above, we conclude that corrugated substrates can be utilized to control the translational velocity of the capsules for a given shear rate. Moreover, when the attraction between the capsule and the corrugated substrate is relatively strong, capsules can be separated accordingly to their size by utilizing the fact that whether a capsule stops or continues moving along the substrate depends critically on the ratio

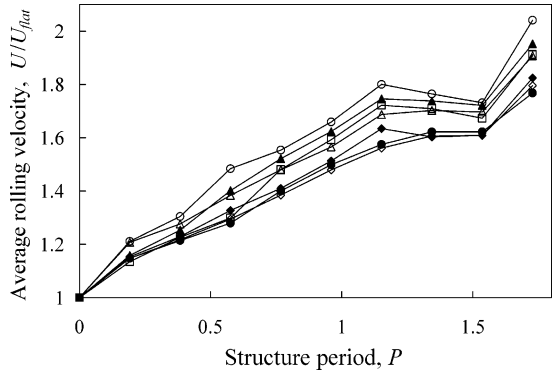

Figure 14. Average rolling velocity of a capsule moving along a corrugated substrate with $E = 1$ vs the pattern period for varying Φ and Ca: (◇) Ca = 2.7×10^{-4} and Φ = 0.06; (●) Ca = 2.7×10^{-4} and Φ = 0.12; (△) Ca = 4×10^{-4} and Φ = 0.12; (◆) Ca = 5.3×10^{-4} and Φ = 0.12; (□) Ca = 4×10^{-4} and Φ = 0.23; (▲) Ca = 5.3×10^{-4} and Φ = 0.23; (○) Ca = 8×10^{-4} and Φ = 0.23.

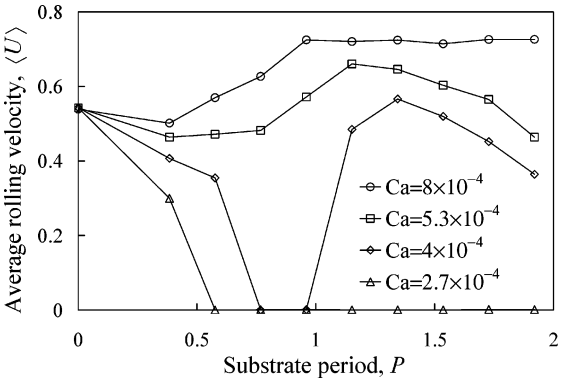

Figure 15. Average rolling velocity of a capsule moving along a substrate with posts vs the pattern period for varying Ca. Here, Φ = 0.58.

between the size of the asperities and the radius of the capsule (as seen in Figure 12).

Substrate with Posts. Finally, we discuss the effect of compliant posts on the motion of capsules along the substrate. For self-propelled cells, such substrates were used to probe the cells' inherent mechanical properties.[20] For fluid-driven cells, we find that these deformable posts affect not only the rolling velocity but also the manner in which the cells traverse the surface, leading to a "crawling", "walking", or "jumping" motion. In our simulations, the respective width and height of the posts are fixed at four and nine lattice spring units, while the period P of the substrate topology is varied. Just as for the corrugated substrates, we fix E to one, which, because of their shape, still yields fairly deformable posts (see Figures 16, 17). The capsules are attracted to only the tops of the posts with an interaction strength Φ of 0.58. (We note that this type of chemical decoration of the posts can be experimentally achieved; Chen et al.[19] were able to selectively bind a protein to only the tops of the pillars, so that the cells were attached only to these particular regions.)

In the ensuing discussion, we first characterize the average rolling velocity on a substrate with posts. Figure 15 summarizes the results for a large range of Ca and P, where the intersection with the y-axis ($P = 0$) represents the flat, uniform substrate. For $P < 0.5$, the capsule rolls for all Ca within the range considered here, albeit with a rolling velocity that decreases with increasing P (for a given value of Ca). For these values of P, the capsule is always in contact with several posts, and the substrate behaves essentially as a flat, uniform, compliant surface (Figure 6a for Φ ≥0.23). (However, as compared to the flat surface, an additional amount of energy is dissipated through the oscillations of the posts that are due to the rolling motion of the capsule.)

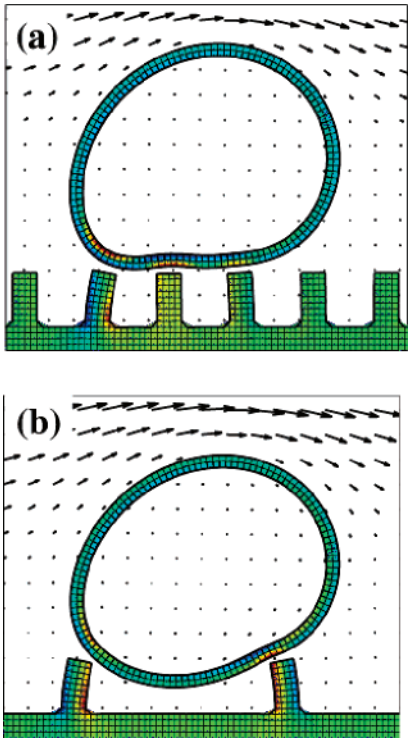

Figure 16. Snapshots of capsules that stop on a substrate with posts for Ca = 2.7×10^{-4}, Φ = 0.58, and $E = 1$: (a) P = 0.576; (b) $P = 1.728$. The colors are as in Figure 4 with δ = 0.02 for both the capsule shell and the substrate.

For P larger than roughly half the capsule radius, the capsule either rolls or stops depending on both Ca and P (compare this to Figures 9 and 12). To help visualize the structure of a capsule that is effectively pinned by the posts, in Figure 16, we show two snapshots of capsules whose motion is arrested by the substrate. Figure 17 shows a series of snapshots of capsules that keep moving along the substrate. Figure 15 clearly indicates that stopped capsules can once again be made to roll by increasing the shear rate. In other words, as in the case of the mechanically patterned and corrugated surfaces, for a fixed surface architecture, variations in γ can be harnessed to either arrest a moving capsule or release a stationary one. Once stopped, a capsule keeps rotating with a constant angular velocity, driven by the applied shear flow.

A remarkably unique aspect provided by the posts is seen in Figure 17, which shows that as a function of the separation between the posts, the capsules can undergo a crawling, walking, or jumping motion. In particular, for $P < 0.7$, the fluid-driven capsule is always supported by at least two posts (Figure 17a). Although the capsule rolls along the surface, its shape barely changes, even though the velocity varies periodically, as shown in Figure 18a,b, where we decompose the velocity into its respective horizontal and vertical components to provide greater insight into the capsule's motion. Hence, the capsule is essentially "crawling" along the substrate.

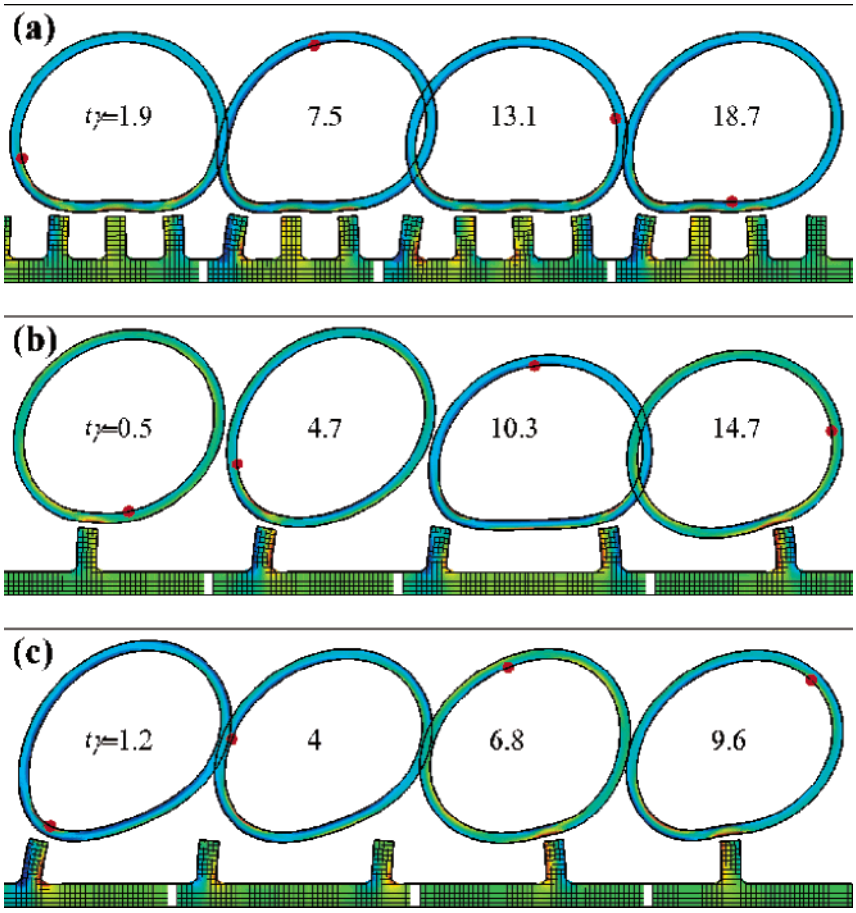

Figure 17. Snapshots of capsule rolling on a substrate with posts for different Ca and P: (a) $P = 0.576$ and $\mathrm{Ca} = 4 \times 10^{-4}$ ("crawling" regime); (b) $P = 1.728$ and $\mathrm{Ca} = 4 \times 10^{-4}$ ("walking" regime); (c) $P = 1.728$ and $\mathrm{Ca} = 8 \times 10^{-4}$ ("jumping" regime). Here, $\Phi = 0.58$ and $E = 1$. The colors are as in Figure 4 with $\delta = 0.02$ for both the capsule shell and the substrate. The time t is measured from the moment that the capsule's center of mass passes the leading edge of a post.

For $1 < P < 2$, the capsule's motion is qualitatively different for different Ca. For small Ca, the capsule is always in contact with at least one post. Starting from a point in time when the capsule is attached to only one post, it will rotate around the post tip due to the applied shear flow, until it touches the next post. If the shear rate is too low to detach the capsule from the first post, it will remain stuck (Figure 16b). Otherwise, the capsule detaches and rotates around the second post, whereupon the entire cycle is repeated (Figure 17b). Such a "walking" motion takes place for $\mathrm{Ca} \leq 4 \times 10^{-4}$. This regime is characterized by substantial variations in the capsule's shape (Figure 17b), large fluctuations in its velocity, which varies more than 20-fold during each complete cycle (Figure 18a,b), and large variations in the capsule's center-of-mass position above the substrate (Figure 18c).

Increasing Ca even further leads to a "jumping" motion, where the capsule disengages from the first post, spends a part of its motion in free flight, and then binds again with the surface (Figure 17c). A similar motion, referred to as "tumbling", was also observed in experiments of rolling leukocytes.[38] The variations in the capsule's shape (Figure 18c) and velocity (Figure 18a,b) are less dramatic for "jumping" than for "walking". In addition, the average velocity of the capsule is practically independent of P and larger than that for a flat, uniform substrate with the same stiffness (Figure 15). Increasing P beyond 2 eliminates the walking regime; the capsule stops, skips, or detaches in order of increasing shear rate.

Comparison of Parameters with Experimental Values. We find that the capsule dynamics is governed by dimensionless groups of particular parameters rather than by the specific values chosen in our simulations. For example, the behavior of the system is influenced by the capillary number, $\mathrm{Ca} = \gamma\mu R/E_c h$; that is, for a fixed Ca, decreasing γ has the same effect as increasing E_c. By expressing the data in terms of such dimensionless numbers, we can provide more flexible guidelines for potential experimental studies. In the case of the capillary number, the experimentalist is free to choose, for instance, a combination of capsule sizes, Young's modulus, and shell thickness that will result in the specified ratio. In the studies presented here, we examined phenomena that span the range of Ca of $10^{-3}-10^{-4}$ since this range yielded the most intriguing behavior and, just as importantly, is relevant to a number of experimental systems, which are described below.

We first consider an example of polyelectrolyte microcapsules[3] that are propelled by an applied shear in an aqueous solution whose viscosity is $\mu \approx 10^{-3}$ kg/(m s) and density is $\rho \approx 10^3$ kg/m^3. The elasticity of the microcapsule's shell (membrane) is on the order of 0.1−1 GPa,[3c,39,40] and these elastic properties are found to be independent of the speed of deformation.[40] (We note that the Young's modulus of the membrane can be tailored by varying the salt concentration in the solution[41] or the solvent temperature.[42]) In typical flow experiments within a microchannel, the shear rate can be up to $\gamma \approx 10^3-10^4$ s^{-1}.[43] If we take experimentally realistic values

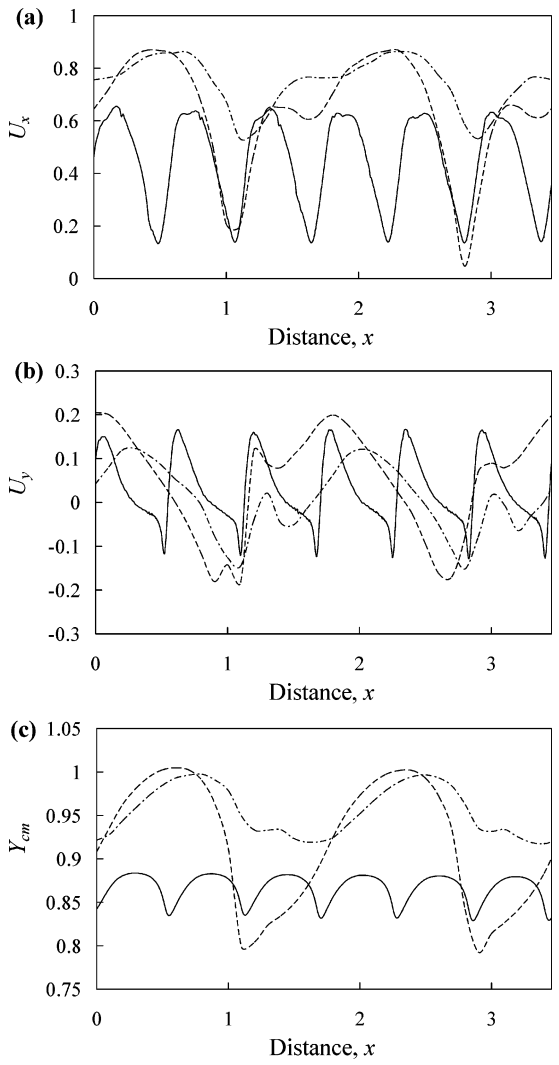

Figure 18. (a) Horizontal and (b) vertical components of rolling velocity and (c) vertical position of the capsule's center of mass vs the distance along the substrate. The solid, dashed and dash−dotted lines are for the capsules in Figure 17a−c, respectively.

of the membrane thickness h to be about 50 nm for a 50 μm capsule,[39] we then obtain Ca $\sim 10^{-4}$, which is in the range considered in the simulations.[44]

A polyelectrolyte coating on the substrate can be utilized to produce an adhesive interaction between the microcapsule and the substrate. The total adhesion energy can be estimated to be on the order of $w \sim 10^{-14}$J/capsule,[45] while the interaction range is roughly $\kappa \sim 10^{-8}-10^{-7}$m.[46] Recall that we define a dimensionless interaction strength $\Phi = \epsilon N/E_c h\kappa^2$; if we set w equal to ϵN and take $E_c h$ from the example above (0.1−1 GPa × 50 nm), we find that Φ is on the order of unity. The latter value is in the range of the parameters considered in our simulations. Moreover, experiments show that the adhesion interaction can be tuned by varying the thickness of the capsule wall.[47] In addition, microcontact printing[48] can be used to produce a chemically patterned coating on the substrate with a period that is on the order of a micrometer or even smaller,[49] allowing for a variation of the net adhesive force that acts on a single capsule.[50]

As noted in the previous section of the paper, recent advances in soft lithography permit the fabrication of mechanically[19] and topographically patterned substrates, which contain regular saw tooth patterns[36] or regular arrays of compliant posts.[19] A thick polymer film with a Young's modulus as low as 10−20 kPa can be patterned by standard lithographic techniques.[51] Given a range of $E_c \sim 0.1-1$ GPa and the above values of E_s, one can obtain a ratio of $E \ll 1$, as considered in Figures 4b,d and 7. Again, to facilitate comparison with our simulations, experimentalists can vary the substrate dimension to fix the ratio $h_s E_s/hE_c$ to be the same as that in the simulations. Here, h_s is the substrate thickness in the case of the mechanically patterned substrate, while for the substrate with posts, h_s is the post thickness.

As noted in the Introduction, the model is also appropriate for modeling the interactions between leukocytes and a substrate. Leukocytes have a cytoskeleton that serves to maintain the spherical shape of the cell, and these cells have in fact been modeled as fluid-filled elastic shells. In such modeling studies, researchers typically use an effective membrane stiffness that lies in the range 0.01−0.3 N/m.[16,18] The shear rate in the blood vessels is about $\gamma \approx 100-500$ s^{-1}. Thus, for leukocytes with radii of the order of 5 μm in an aqueous solution, one obtains typical values of the capillary number Ca $\sim 10^{-4}$, which again is in the range of our numerical simulations. We, therefore, expect that qualitatively similar behavior can be observed in experimental studies on the interactions between leukocytes and the endothelial layer or in studies where ex vivo leukocytes are used as the fluid-driven capsules (and the imposed shear rate is comparable to $\gamma \approx 100-500$ s^{-1}, so that Ca remains in the range cited above).

In the case of short-chain liposomes, comparison with the simulations presented here is a more difficult task, mainly for two particular reasons. First, the lipid bilayer is nearly incompressible and has an extremely low bending modulus. Thus, both the total volume of the vesicle, V, and its surface area, S, are conserved. This means that the reduced volume of a vesicle $V_r = V/(4/3)\pi(S/4\pi)^{3/2}$ is a constant, which is usually somewhat less than unity.[24] In contrast, in our simulations, the initial reduced volume is unity and becomes reduced due to shell deformation and extension as the capsule interacts with the imposed flow and substrate. Second, the lipid membranes are highly fluidic and, therefore, cannot be modeled in a straightforward manner as an elastic medium. On the other hand, long-chain liposomes, or polymersomes, can more readily be described in terms of LSM, since the membranes are composed of high-molecular-weight polymers. If the degree of polymerization is above the entanglement length, the fluidity of the membrane is significantly reduced;[4b] furthermore, the polymers in the membrane can be cross-linked to enhance the membrane durability.[4] In the latter cases, the membrane can be appropriately modeled by the LSM. Additionally, polymersomes can be decorated with specific ligands to induce an adhesive interaction with the substrate.[52]

Nonetheless, in some cases, a qualitative comparison can be made between lipid vesicles and our simulations as long as V_r of the vesicle is close to that of our deformed capsule. Indeed, the shapes of the microcapsule shown in Figure 4 are similar to those obtained in the experiments with giant lipid vesicles reported by Abkarian et al.[24a] and more recently by Abkarian and Viallat.[24b,53,54]

Finally, we note that in a 3D system additional effects can arise that affect the shape of the capsule and the way it moves; such effects might not be captured in our 2D model. Nevertheless, we anticipate that the phenomena reported herein can be experimentally examined for the range of the dimensionless parameters described above.

Conclusions

In summary, we integrated two mesoscale approaches—the lattice Boltzmann model for fluid dynamics and the lattice spring model for the micromechanics of solids—to create an efficient computational scheme for examining the behavior of fluid-driven capsules on compliant surfaces. Each capsule is composed of a bounding elastic shell and an encapsulated fluid. Such fluid-filled elastic shells serve as models for biological cells, such as leukocytes, or polymeric microcapsules. Using the hybrid LBM/LSM model, we undertook the first computational studies to determine how the compliance and topography of the surface affect the motion of the capsules.

For the case of a flat surface with uniform mechanical properties, we observed that the capsules undergo a rolling motion along the substrate. This behavior is also observed experimentally for leukocytes moving in blood vessels. We varied the value of the spring constants in the LSM lattice that makes up the substrate and found that the stiffness of the surface plays a significant role in dictating the translational velocity of the rolling capsules. In particular, decreases in the stiffness of the surface lead to significant decrease in the velocity.

We also examined the effect of mechanically and topologically patterned surfaces on the dynamic behavior of the capsules. In the case of the mechanically patterned surfaces, we focused on substrates that encompass alternating regions of soft and hard domains; the topographically patterned surfaces were corrugated or contained regular arrays of compliant posts. All these substrates can be fabricated experimentally, with well-defined, micron-scale features.[19,36] Our findings reveal that these substrates can be harnessed to halt the motion of the capsules at specific locations on the surface. With a small increase in the shear rate, the capsules can be made to resume their motion. In effect, these surfaces permit the capsules to be driven to a particular surface site, where they can be analyzed or manipulated, and then moved to the next station for further processing. This level of control was achieved simply by a coupling of a patterned surface and an imposed flow field; it did not require the complicated circuitry that underlies several droplet-based microfluidic devices.[2]

In addition to providing "stop" and "go" instructions, the system of imposed flow and topographically patterned surfaces modulates the capsule's motion. In particular, by varying the amount of surface roughness, i.e., the size of the ridges for corrugated substrates, we obtain significant control over the translational velocity of a capsule for a given shear rate. This behavior is reminiscent of the phenomena seen with superhydrophobic surfaces, where asperities can propel the motion of a droplet on the surface.[37]

In the case of surfaces containing a regular array of posts, we find that as a function of the post separation, a capsule can be made to "crawl", "walk", or "jump" along the surface. The controlled "walking" can be utilized to promote the intermixing of reagents that are encapsulated within the microcapsules.

Finally, for topographically patterned surfaces with a relatively strong interaction between the capsule and the substrate, capsules can be separated accordingly to their size by utilizing the fact that whether a capsule stops or continues moving along the substrate depends critically on the ratio between the size of the asperities and the radius of the capsule.

The ability to manipulate the capsule's dynamic behavior in this manner can allow researchers to perform various well-controlled biological assays.[22] The findings also yield guidelines for creating an array of maneuverable microcapsules, which serve as microreactors. Because of the versatility and robustness of the microcapsules, this system can provide advantages over more traditional fluid stream or droplet-based lab-on-a-chip systems. In particular, a broad class of materials can readily be encapsulated within the core of the capsules,[6] and the entire assembly offers significant storage stability. Furthermore, chemical reactions, such as polymerization, can be carried out within these carriers[8] and the products effectively stored until needed (i.e., at a given time, external light or heat can be applied in order to rupture the capsule and allow the contents to be analyzed or processed).

It is important to note that recent advances in the fabrication of polymersomes[4] and chemically tailored polymeric microcapsules[6−12] means that researchers have access to mechanically tough and versatile capsules. Furthermore, advances in soft lithography allow researchers to create patterned surfaces with highly regular, microscopic features. Thus, our findings on the behavior of microcapsules on a variety of substrates can be experimentally tested and can provide the needed design rules for creating the optimal assemblies of microcapsules, surfaces, and host fluids.

Acknowledgment. The authors gratefully acknowledge discussions with Dr. G. A. Buxton and Dr. A. Fery. This work was supported by DOE. Partial salary support for some of the work was provided by ONR to Rolf Verberg.

References and Notes

(1) Haswell, S. J.; Middleton, R. J.; O'Sullivan, B.; Skelton, V.; Watts, P.; Styring, P. *Chem. Commun.* **2001**, *5*, 391−398.

(2) See for example: (a) Burns, M. A.; Johnson, B. N.; Brahmasandra, S. N.; Handique, K.; Webster, J. R.; Krishnan, M.; Sammarco, T. S.; Man, P. M.; Jones, D.; Heldsinger, D.; Mastrangelo, C. H.; Burke, D. T. *Science* **1998**, *282*, 484−487. (b) Hosokawa, K.; Fujii, T.; Endo, I. *Anal. Chem.* **1999**, *71*, 4781−4785. (c) Darhuber, A. A.; Davis, J. M.; Reisner, W. W.; Troian, S. M. *Micro Total Analysis Systems 2001*; Ramsey, J. M., van den Berg, A., Eds.; Kluwer Academic Publishers: Dordrecht, 2001, pp 244−246. (d) Cho, S. K.; Moon, H.; Kim, C.-J. *J. Microelectromechan. Syst.* **2003**, *12*, 70−80. (e) Pollack, M. G.; Shenderov, A. D.; Fair, R. B. *Lab Chip* **2002**, *2*, 96−101. (f) Schwartz, J. A.; Vykoukal, J. V.; Gascoyne, P. R. C. *Lab Chip* **2004**, *4*, 11−17. (g) Velev, O. D.; Prevo, B. G.; Bhatt, K. H. *Nature (London)* **2003**, *426*, 515−516. (h) Srinivasan, V.; Pamula, V. K.; Pollack, M. G.; Fair, R. B. *Micro Total Analysis Systems 2003*; Kluwer Academic Publishers: Dordrecht, 2003; pp 1287−1290.

(3) See for example: (a) Gao, C. Y.; Leporatti, S.; Moya, S.; Donath, E.; Möhwald, H. *Langmuir* **2001**, *17*, 3491−3495. (b) Lulevich, V. V.; Radtchenko, I. L.; Sukhorukov, G. B.; Vinogradova, O. I. *Macromolecules* **2003**, *36*, 2832−2837. (c) Fery, A.; Dubreuil, F.; Mohwald, H. *New J. Phys.* **2004**, *6*, 18. (d) Vinogradova, O. I. *J. Phys.: Condens. Matter* **2004**, *16*, R1105−R1134. (e) Peyratout, C. S.; Dahne, L. *Angew. Chem., Int. Ed.* **2004**, *43*, 3762−3783.

(4) (a) Discher, B. M.; Won, Y.-Y.; Ege, D. S.; Lee, J. C.-M.; Bates, F. S.; Discher, D. E.; Hammer, D. A. *Science* **1999**, *284*, 1143−1146. (b) Discher, D. E.; Eisenberg, A. *Science* **2002**, *297*, 967−973 and references therein.

(5) Most of the examples cited below involve microcapsules made from layer-by-layer deposition of polyelectrolytes, since these systems have been very well characterized and highly utilized. There are, however, numerous other examples of tough microcapsules (see ref 3 above, for example).

(6) See for example: (a) Caruso, F.; Trau, D.; Möhwald, H.; Renneberg, R. *Langmuir* **2000**, *16*, 1485−1488. (b) Moya, S.; Sukhorukov, G. B.; Auch, M.; Donath, E.; Möhwald, H. *J. Colloid Interface Sci.* **1999**, *216*, 297−302. (c) Shchukin, D. G.; Radtchenko, I. L.; Sukhorukov, G. B. *Mater. Lett.* **2003**, *57*, 1743−1747. (d) Voigt, A.; Buske, N.; Sukhorukov, G. B.; Antipov, A. A.; Leporatti, S.; Lichtenfeld, H.; Bäumler, H.; Donath, E.; Möhwald, H. *J. Magn. Magn. Mater.* **2001**, *225*, 59−66.

(7) See for example: Ibarz, G.; Dähne, L.; Donath, E.; Möhwald, H. *Adv. Mater.* **2001**, *13*, 1324−1327.

(8) Dähne, L.; Leporatti, S.; Donath, E.; Möhwald, H. *J. Am. Chem. Soc.* **2001**, *123*, 5431−5436.

(9) Antipov, A. A.; Sukhorukov, G. B.; Leporatti, S.; Radtchenko, I. L.; Donath, E.; Möhwald, H. *Colloids Surf. A* **2002**, *198*, 535−541.

(10) See for example: (a) Volodkin, D. V.; Balabushevitch, N. G.; Sukhorukov, G. B.; Larionova, N. I. *STP Pharm. Sci.* **2003**, *13*, 163−170. (b) Antipov, A. A.; Sukhorukov, G. B.; Möhwald, H. *Langmuir* **2003**, *19*, 2444−2448. (c) Petrov, A. I.; Gavryushkin, A. V.; Sukhorukov, G. B. *J. Phys. Chem. B* **2003**, *107*, 868−875. (d) Kim, B.-S.; Vinogradova, O. I. *J. Phys. Chem. B* **2004**, *108*, 8161−8165.

(11) Kim, B. S.; Lebedeva, O. V.; Koynov, K.; Gong, H.; Glasser, G.; Lieberwith, I.; Vinogradova, O. I. *Macromolecules* **2005**, *38*, 5214−5222.

(12) (a) Park, M.-K.; Deng, S.; Advincula, R. C. *Langmuir* **2005**, *21*, 5272−5277. (b) Haque, E.; Lentz, B. R. *Biophys. J.* **2005**, *88*, 67A−67A. (c) Evans, K. O.; Lentz, B. R. *Biophys. J.* **2001**, *80*, 1766. (d) Wienreb, G.; Lentz, B. R. *Biophys. J.* **2004**, *86*, 46A−46A. (e) Gao, L.; Shi, L.; Zhang, W.; An, Y.; Liu, Z.; Li, G.; Meng, Q. *Macromolecules* **2005**, *38*, 4548−4550.

(13) Succi, S. *The Lattice Boltzmann Equation for Fluid Dynamics and Beyond*; Clarendon Press: Oxford, 2001.

(14) (a) Ladd, A. J. C.; Kinney, J. H.; Breunig, T. M. *Phys. Rev. E* **1997**, *55*, 3271−3275. (b) Ladd, A. J. C.; Kinney, J. H. *Physica A* **1997**, *240*, 349−360.

(15) Buxton, G. A.; Verberg, R.; Jasnow, D.; Balazs, A. C. *Phys. Rev. E* **2005**, *71*, 056707.

(16) (a) Dong, C.; Cao, J.; Struble, E. J.; Lipowsky, H. H. *Ann. Biomed. Eng.* **1999**, *27*, 298−312. (b) Jadhav, S.; Eggleton, C. D.; Konstantopoulos, K. *Biophys. J.* **2005**, *88*, 96−104 and references therein.

(17) Marella, S. V.; Udaykumar, H. S. *Phys. Fluids* **2004**, *16*, 244−264.

(18) (a) Krasik, E. F.; Hammer, D. A. *Biophys. J.* **2004**, *87*, 2919−104. (b) Khismatullin, D. B.; Truskey, G. A. *Microvasc. Res.* **2004**, *68*, 188−202 and references therein.

(19) Chen, C. S.; Jiang, X.; Whitesides, G. M. *MRS Bull.* **2005**, *30*, 194−201.

(20) Lemmon, C. A.; Sniadecki, N. J.; Ruiz, S. A.; Tan, J. T.; Romer, L. H.; Chen, C. S. *Mech. Chem. Biosys.* **2005**, *2*, 1−16.

(21) Gray, D. S.; Tien, J.; Chen, C. S. *J. Biomed. Mater. Res.* **2002**, *66A*, 605−14.

(22) Lahann, J.; Langer, R. *MRS Bull.* **2005**, *30*, 185−188.

(23) Buxton, G.; Balazs, A. C. *J. Chem. Phys.* **2002**, *117*, 7649−7658 and references therein.

(24) (a) Abkarian, M.; Lartigue, C.; Viallat, A. *Phys. Rev. E* **2002**, *63*, 041906−7. (b) Abkarian, M.; Viallat, A. *Biophys. J.* **2005**, *89*, 1055−1066.

(25) (a) Perktold, K.; Rappitsch, G. *J. Biomech.* **1995**, *28*, 845−856. (b) Penrose, J. M. T.; Staples, C. J. *Int. J. Numer. Methods Fluids* **2002**, *40*, 467−478. (c) Teixeira, P. R. F.; Awruch, A. M. *Comput. Fluids* **2005**, *34*, 249−273 and references therein.

(26) Frisch, U.; d'Humières, D.; Hasslacher, B.; Lallemand, P.; Pomeau, Y.; Rivet, J.-P. *Complex Syst.* **1987**, *1*, 649−707.

(27) d'Humières, D.; Ginzburg, I.; Krafczyk, M.; Lallemand, P.; Luo, L.-S. *Philos. Trans. R. Soc. A* **2002**, *360*, 437−451.

(28) Tuckerman, M.; Berne, B. J.; Martyna, G. J. *J. Chem. Phys.* **1992**, *97*, 1990−2001.

(29) (a) Schwartz, L. M.; Feng, S.; Thorpe, M. F.; Sen, P. N. *Phys. Rev. B* **1985**, *32*, 4607−4617. (b) Arbabi, S.; Sahimi, M. *Phys. Rev. B* **1990**, *41*, 772−775.

(30) Bouzidi, M.; Firdaouss, M.; Lallemand, P. *Phys. Fluids* **2001**, *13*, 3452−3459.

(31) The derivation in two dimensions proceeds along the same lines as that for three dimensions as discussed in detail in ref 15. This results in a solution in terms of integer Bessel functions as opposed to spherical Bessel functions. The solution is then solved numerically.

(32) Sangani, A. S.; Acrivos, A. *Int. J. Multiph. Flow* **1982**, *8*, 193−206.

(33) Stone, H. A. *Annu. Rev. Fluid Mech.* **1994**, *26*, 65−102.

(34) (a) Lawrence, M. B.; Springer, T. A. *J. Immunol.* **1993**, *151*, 6338−6346. (b) Lawrence, M. B.; Springer, T. A. *Cell* **1991**, *65*, 859−873.

(35) Cantat, I.; Misbah, C. *Phys. Rev. Lett.* **1999**, *83*, 880−883.

(36) Okayasu, T.; Zhang, H.-L.; Bucknall, D. G.; Briggs, G. A. D. *Adv. Funct. Mater.* **2004**, *11*, 1081−1088.

(37) (a) Öner, D.; McCarthy, T. J. *Langmuir* **2000**, *16*, 7777−7782. (b) Lafuma, A.; Quéré, D. *Nat. Mater.* **2003**, *2*, 457−460. (c) Dupuis, A.; Yeomans, J. M. *Langmuir* **2005**, *21*, 2624−2629 and references therein.

(38) King, M. R.; Kim, M. B.; Sarelius, I. H.; Hammer, D. A. *Microcirculation* **2003**, *10*, 401−409.

(39) Dubreuil, F.; Elsner, N.; Fery, A. *Eur. Phys. J. E* **2003**, *12*, 215−221.

(40) Elsner, N.; Dubreuil, F.; Weinkamer, R.; Wasicek, M.; Fischer, F. D.; Fery, A. *Prog. Colloid Polym. Sci.,* in press.

(41) Heuvingh, J.; Zappa, M.; Fery, A. *Langmuir* **2005**, *21*, 3165−3171.

(42) Mueller, R.; Kohler, K.; Weinkamer, R.; Sukhorukov, G.; Fery, A. *Macromolecules*, in press.

(43) Stone, H. A.; Stroock, A. D.; Ajdari, A. *Annu. Rev. Fluid Mech.* **2004**, *36*, 381−411.

(44) The polyelectrolyte membrane is typically penetrable to solvent, whereas in our simulations we consider an impermeable membrane. However, the diffusion coefficient through the polyelectrolyte microcapsule's wall is less than 10^{-15} cm^2/s for entities with molecular weight less than 1 kDa.[3c] We, therefore, expect that under typical experimental conditions the capsule can be viewed as impenetrable, implying that it conserves its volume during the time of the experiment.[3d] (We can estimate the typical experimental time to be of the order of $100\gamma \sim 1$ s, by taking the characteristic velocity γR and substrate length $\sim 100R$.) Furthermore, the permeability can be controlled by varying the pH or salt concentration of the solution[10] and greatly reduced by assembling additional multilayers onto the capsule.[3e] Our model can be further extended to account for the effect of solvent diffusion through the capsule wall by the appropriate change in the boundary conditions.

(45) Nolte, M.; Fery, A. *Langmuir* **2004**, *20*, 2995−2998.

(46) Bosio, V.; Dubreuil, F.; Bogdanovic, G.; Fery, A. *Colloids Surf. A: Physicochem. Eng. Aspects* **2004**, *243*, 147−155.

(47) Elsner, N.; Dubreuil, F.; Fery, A. *Phys. Rev. E* **2004**, *69*, 031802−6.

(48) Kumar, A.; Whitesides, G. M. *Science* **1994**, *263*, 60−62.

(49) Stamou, D.; Duschl, C.; Delamarche, E.; Vogel, H. *Angew. Chem., Int. Ed.* **2003**, *42*, 5580−5583.

(50) We note that such chemical patterning could produce an effect similar to that of the mechanical patterning; i.e., the presence of chemical variations could cause microcapsules to stop at the end of an adhesive patch when the period of the pattern is comparable to the capsule size. When the pattern period is larger than the capsule, the capsule can detach from the substrate during its motion along the nonadhesive patch due to the hydrodynamic lift force. For this reason, the mechanical patterning could be preferable in controlling the capsules' traffic.

(51) Schwarz, U. S.; Balaban, N. Q.; Riveline, D.; Bershadsky, A.; Geiger, B.; Safran, S. A. *Biophys. J.* **2002**, *83*, 1380−1394.

(52) Lin, J. J.; Bates, F. S.; Hammer, D. A.; Silas, J. A. *Phys. Rev. Lett.* **2005**, *95*, 026101−4.

(53) Liposomes can also be decorated with specific ligands to induce an adhesive interaction with the substrate.[55] In particular, Cuvelier et al.[55] experimented with lipid vesicles decorated with streptavidin on a glass substrate covered with biotin. They found the lipid vesicles spread and firmly adhere to the biotin-activated substrate even in the presence of a shear rate of 14.5 s^{-1}, while the shape of the vesicle was a truncated sphere (similar to that shown in Figure 4a where $\mathrm{Ca} = 8 \times 10^{-4}$ and $\Phi = 1.15$). Assuming that that vesicle membrane is stretched and the stretching elastic modulus is of the order of 0.1 N/m, we can estimate the capillary number for the experiment reported by Cuvelier et al.[55] to

be about Ca $\sim 10^{-6}$. This low capillary number can explain why the shape of the vesicle in the experiment remains nearly symmetrical without any evident deformation due to the shear flow. Comparing the shape of the vesicle with our numerical results, we can conclude that there is a rather strong adhesion between the vesicle and the substrate such that $\Phi > 1$. Our simulations indicate that in such conditions even a small gradient in the adhesive strength along the substrate (receptor density in the experiment) can prevent the vesicle from rolling. Moreover, due to the fluidic nature of a lipid membrane, the lipids that are not involved in adhesion will flow around the bound lipids, which are in firm adhesion with the substrate receptors. As a result, the force acting to disconnect the bound lipids is reduced[56] and the vesicle remains stuck. This should not be the case for the cross-linked polymersomes, where the membrane exhibits significant shear rigidity.

(54) It should be noted that the apparent elastic modulus of a lipid membrane can be written as a superposition of the entropy-dominated effects due to the microscopic membrane fluctuations that persist at all levels of tension and the direct expansion of the membrane.[57] Thus, the apparent elasticity is a nonlinear function of membrane tension. Although in our current implementation we use a linear law for the elastic membrane, it is possible to extend our model to mimic the nonlinear dynamics of lipid membranes by changing the LSM to reflect the apparent elasticity of the lipid membrane.

(55) Cuvelier, D.; Vezy, C.; Viallat, A.; Bassereau, P.; Nassoy, P. *J. Phys.: Condens. Matter* **2004**, *16*, S2427−S2437.

(56) Goldman, A. J.; Cox, R. G.; Brenner, H. *Chem. Eng. Sci.* **1967**, *22*, 637−651.

(57) Evans, E.; Rawicz, W. *Phys. Rev. Lett.* **1990**, *64*, 2094−2097.

MA0516135